# Thermodynamic modeling and design of high-performance adsorption-based atmospheric water harvesting devices

by

Adela Chenyang Li

B.S. in Mechanical Engineering, University of California at Berkeley, 2020

Submitted to the Department of Mechanical Engineering in Partial Fulfillment of the Requirements for the Degree of

Master of Science in Mechanical Engineering

at the
Massachusetts Institute of Technology
September 2022

Author ........................................................................................................................................
Department of Mechanical Engineering
August 15, 2022

Certified by ................................................................................................................................
Evelyn N. Wang
Ford Professor of Engineering and Department Head of Mechanical Engineering
Thesis Supervisor

Accepted by ...............................................................................................................................
Nicolas Hadjiconstantinou
Professor of Mechanical Engineering
Chair, Department Committee on Graduate Theses

# Acknowledgements

I will never be able to express the depth of appreciation and respect I have had for my advisor, Professor Evelyn Wang. I am extremely thankful that she welcomed me to her research group with affirmation and trust (during the deeply uncertain time of the pandemic) and remained an unwavering source of support to me since. I am also utmost grateful for the transformative training I received from Evelyn. She influenced me to focus on developing not only academic knowledge and skills, but also an eye for practical technologies with real world impact. She helped me see the power of teamwork, communication, and resilience, qualities that she always led by example.

Lenan Zhang and Simo Pajovic were extraordinary mentors and friends to me. I am fortunate to have had Lenan as a senior student mentor and received constant support from him in almost every aspect of my life. In terms of research, the bulk of this thesis was completed under his mentorship and led to our first journal paper together as co-authors. In terms of non-research, he was the kind of friend who dropped assorted supplies to my door when I fell sick for covid, just to give an example. Simo has also been above and beyond as my GAME mentor, who always made himself available to his mentees. He was the one that I turned to for advice all the time. It was for him that I had a smooth transition to MIT and stayed afloat through the ups and downs of being a graduate student here. His impeccable work ethic, quick wit, and unlimited love for cats have brought me great joy.

Lastly, I thank my family and friends with all my heart. Love you Baba, Mama, Didi, and Laolao. Love you Ruiyi and Guanqun. Love you Quark (the smallest and highest energy kitten on earth that I am lucky to call mine). Love you Caroline, Steph, Edward and Qian. Love you Michael. And love you my girl, Janice.

# Thermodynamic modeling and design of high-performance adsorption-based atmospheric water harvesting devices

by

Adela Chenyang Li

Submitted to the Department of Mechanical Engineering in Partial Fulfillment of the Requirements for the Degree of

Master of Science in Mechanical Engineering

## Abstract

Water scarcity is a grand global challenge since more than two-thirds of world's population is experiencing water shortage. Atmospheric water harvesting (AWH) addresses this challenge by enabling decentralized freshwater supply in water-stressed and infrastructure-limited areas. Adsorption-based AWH, in particular, overcomes the climate limitations of conventional AWH technologies and has the potential to further expand clean water access to extremely arid regions. Despite innovations in adsorbent materials, however, fundamental understanding of the physical processes involved in the AWH cycle and how material properties impact the theoretical limits of AWH are lacking.

In this thesis, we develop a generalized thermodynamic framework to elucidate the interplay between adsorbent properties and operating conditions for optimal AWH performance. Our analysis considers the temperature-dependence of adsorption, which is critical but has been largely overlooked in past work. Using metal-organic framework (MOF) as an example, we show that the peak energy efficiencies of single-stage and dual-stage AWH devices, after considering temperature-dependent adsorption, increased by 30% and 100% compared with previous work. Moreover, in contrast to common understanding, we show that the adsorption enthalpy of MOFs can also be optimized and further improve the peak energy efficiency by 40%.

To guide the practical design of next-generation adsorption-based AWH devices, we also perform initial modeling and characterization of select subcomponents for enhanced device performance. For atmospheric air delivery, we show that both the Dyson V9 motor fan and miniature drone propellers are powerful and compact solutions. However, after taking the power consumption into account, we identify the Noctua industrial DC fan as the best candidate overall for air supply. In addition, we show that significant heat sink enhancement is needed to maintain the condenser at close to ambient temperature and sustain the high flux of vapor condensation prescribed by high water productivity. This work bridges important knowledge gaps between adsorbent materials development and device design, providing insights toward high-performance adsorption-based AWH technologies.

Thesis Supervisor: Prof. Evelyn N. Wang
Title: Ford Professor of Engineering and Department Head of Mechanical Engineering

# Contents

# List of Figures

# List of Tables

# Chapter 1: Introduction

## 1.1. Motivation

Global water scarcity is affecting two-thirds of the world's population today,[4] making it a leading challenge in the United Nations (UN) Sustainable Development Goals.[5] Atmospheric water harvesting (AWH) technologies address this challenge by enabling decentralized freshwater supply in water-stressed and infrastructure-limited areas. Adsorption-based AWH, in particular, overcomes the climate limitations of conventional AWH technologies and has the potential to further expand clean water access to extremely arid regions. To improve the performance of adsorption-based AWH devices, both the fundamental thermodynamic modeling of ideal AWH processes and the practical design of device subcomponents are crucial.

### 1.1.1. Global water scarcity: primary drivers, metrics, and impact

There are two primary types of water scarcity: physical and economic water scarcity.[6,7] Physical water scarcity describes the lack of available freshwater to meet standard demands, which may include both human water consumption and environmental flow requirements.[4,7] Economic water scarcity, on the contrary, typically refers to the lack of infrastructure to withdraw or distribute available freshwater to the population of concern.[6,7] The present extent of global physical and economic water scarcity is shown in Fig. 1. In general, physical water scarcity affects arid areas such as central Asia and North Africa the most,[8] whereas economic water scarcity primarily impacts undeveloped regions in Latin America and Sub-Saharan Africa.[7]

Not estimated  Physical water scarcity  Economic water scarcity
Little or no water scarcity  Approaching physical water scarcity
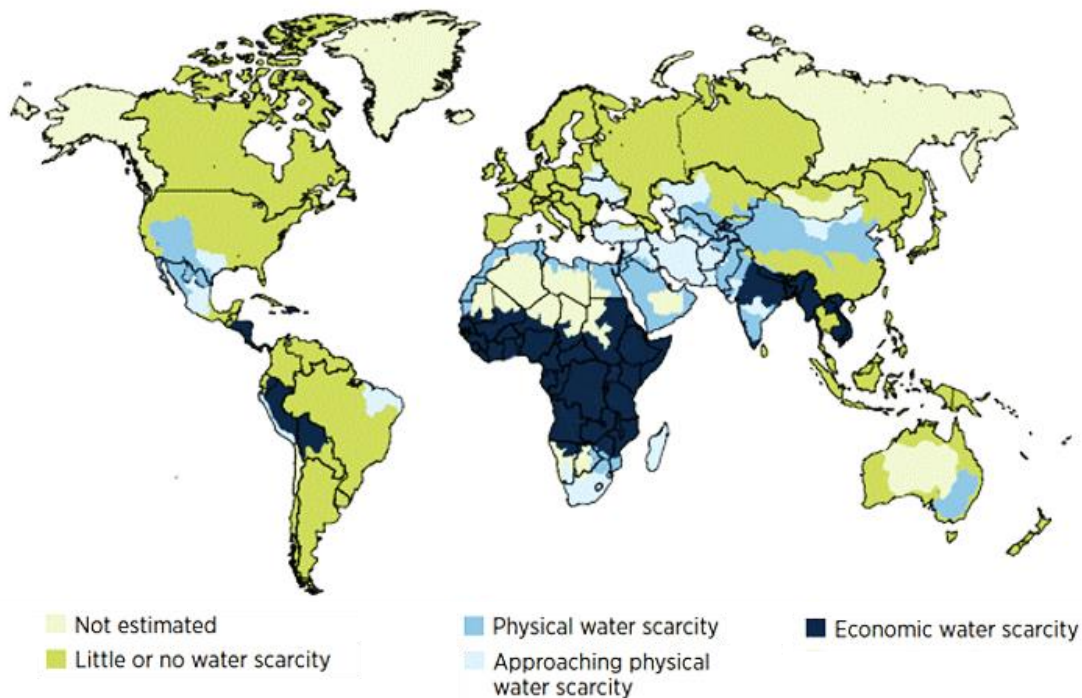
**FIG. 1. Global physical and economic water scarcity, reproduced from the United Nations World Water Development Report 4. WWAP, March 2012.**[6]

Two well-known metrics of water scarcity are the Water Crowding Index (WCI) and Water Stress Index (WSI).[1] WCI is a measure of the annual water resources per capita in a watershed. On the other hand, WSI is a measure of the ratio of water withdrawal to availability. A region is considered water-scarce if the local WCI is smaller than 1000 $m^3$ per capita per year, or if the WSI is greater than 0.4. These two metrics highlight different aspects of water scarcity. WCI highlights the effect of population size or density, whereas WSI depends strongly on the patterns of water consumption.

Water scarcity is, fundamentally, an indicator of the mismatch between freshwater supply and demand.[6,9,10] The key drivers of rising global freshwater demand are the continuous world population growth and economic development.[4,11–13] At the same time, global freshwater supply is decreasing due to key drivers such as surface and groundwater depletion, pollution, and climate change.[1,12,14] Figures 2(a)-(b) show the regions of the world projected to see increase in two water scarcity metrics by 2050 under the effects of climate change.[1]
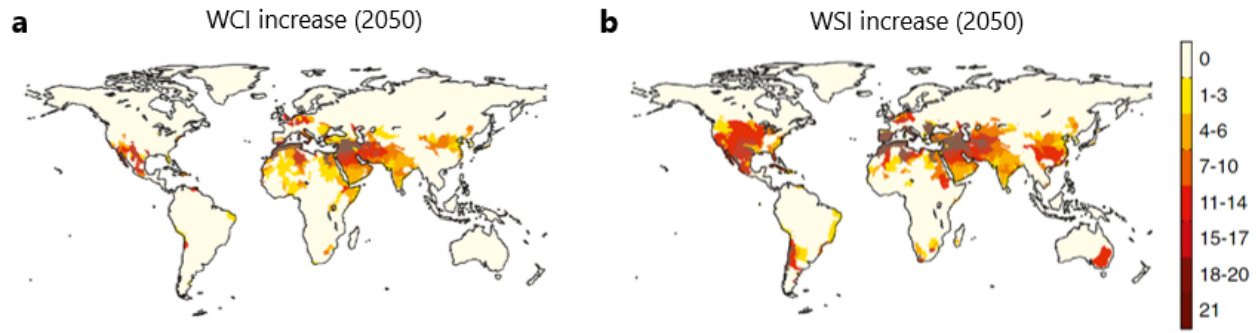
**FIG. 2. Regions of the world projected to see increase in water scarcity by 2050 under climate change, reproduced from Gosling _et al._, _Climatic Change_, 2016.**[1] Water scarcity measured by the (a) Water Crowding Index (WCI) and (b) Water Stress Index (WSI).

The mismatch between freshwater supply and demand has been growing since last century and driving the rapid intensification of water scarcity. Mekonnen _et al._ projected that six billion people will face water scarcity by 2050.[4] Boretti _et al._ illustrated the concurrent increase in clean water demand and decrease in supply both globally and for a group of highly water-scarce countries [Fig. 3].[2] By illustrating the opposing changes in water supply and demand over time, their work also suggests that continued water could escalate into a water crisis when the demand and availability curves intersect. For the group of highly water-scare countries, a water crisis could emerge by as early as 2040.
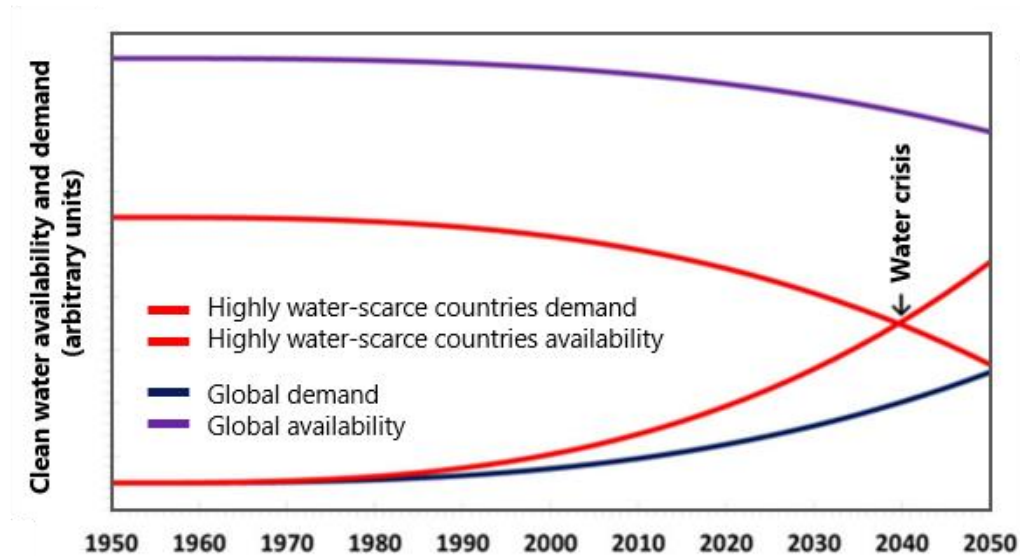
**FIG. 3. Graphical concept of growing freshwater demand and reducing supply, reproduced from Boretti *et al.*, *NPJ Clean Water*, 2019.**[2] Highly water-scarce countries highlighted here include select countries from Asia and Africa.

Beyond the water sector itself, water scarcity also significantly impacts many other aspects of global sustainable development. Around 70% of the world's freshwater is used for irrigation and livestock presently.[6] Therefore, escalating water scarcity is a major threat to global agriculture and food security.[15] The lack of clean water to meet the minimum daily standards for drinking and sanitation also causes critical public health concerns, which are already affecting parts of the world population.[16–18] Furthermore, water scarcity is projected to compromise the global economy according to recent hydrologic-economic models.[19]

### 1.1.2. Harvesting freshwater from the air

Atmospheric water harvesting (AWH) enables decentralized freshwater supply in water-scarce and resource-limited regions of the world by harvesting the water vapor in the air.[20–23] This expands global clean water supply beyond conventional sources, and has potential to address both physical and economic water scarcity.

Two existing AWH technologies are fog harvesting and dewing. Fog harvesting uses a physical mesh to capture saturated water droplets in low-lying clouds [Fig. 4. inset]. The captured droplets drip down the mesh due to gravity and ultimately get collected as clean liquid water. A key advantage of fog harvesting is that it is a fully passive and does not require energy input. Dewing,

on the contrary, involves the active condensation of atmospheric vapor into liquid water. This is achieved by cooling a stream of moist air below the dew point using a refrigeration system [Fig. 4. inset]. The dew point varies with the environment and can be determined from the air temperature and humidity ratio. Dewing is useful when there is no fog present, but it is only feasible when the dew point of the inlet air is above freezing temperature (0°C). Figure 4 shows a psychrometric chart that illustrates the operating regimes of fog harvesting and dewing AWH. In general, relatively high RH conditions are required for both fog harvesting (100% RH) and dewing (>40% RH below 27°C). The climate limitations of these existing AWH technologies are major barriers to their applications.
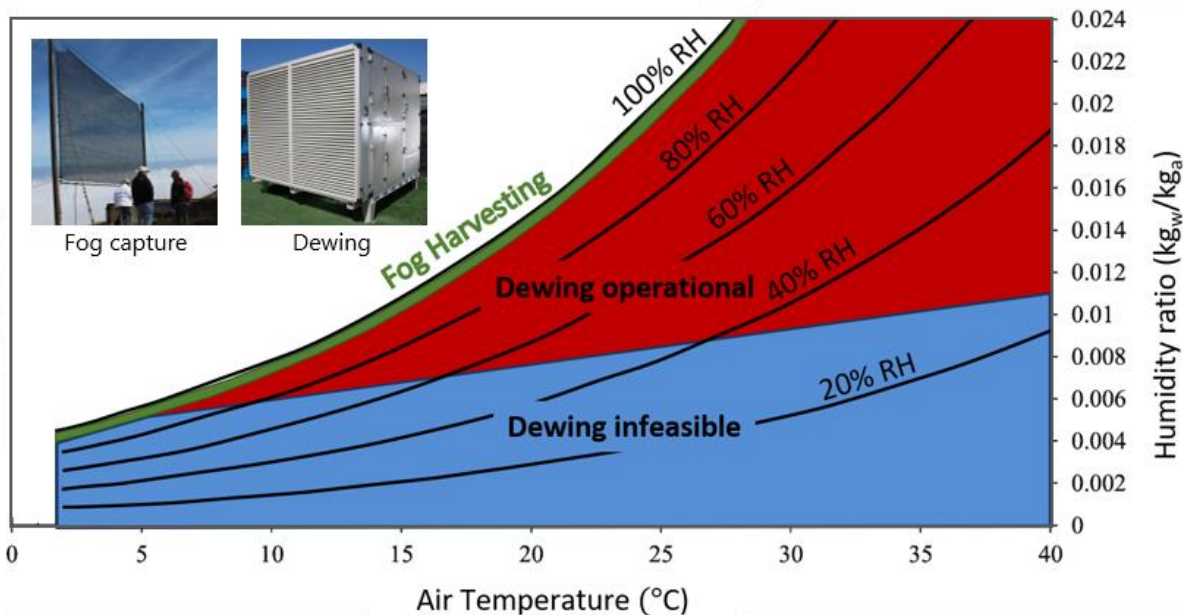


**FIG. 4. Operating regimes of existing AWH technologies, reproduced from LaPotin, MIT SM Thesis, 2019.**[3]

## 1.2. Adsorption-based atmospheric water harvesting

Adsorption-based AWH has the potential to extend decentralized freshwater supply to extremely arid regions of the world, where fog capture and dewing are infeasible.[24–28] Developing high-performance AWH technology is a multi-scale challenge that relies on key innovations ranging from materials to device.

### 1.2.1. Fundamental working principles and recent advances

Adsorption is a widely occurring phenomenon in nature and has diverse engineering applications.[29–32] It describes the physically adhesion of atoms, ions, or molecules to a surface.[33] The surface is called the *adsorbent*, whereas the atoms, ions, or molecules being adsorbed are called *adsorbates*. Adsorption occurs spontaneously and is primarily driven by the reduction in adsorbent surface energy following its physical bonding with the adsorbate. It is important to note that adsorption is strictly a surface phenomenon and fundamentally differs from *absorption*, which involves the fluidic transport of adsorbates through the bulk of the adsorbent.

Porous materials are generally great adsorbents because they exhibit large adsorption surface and fast transport kinetics within the pores. Figures 5(a)-(b) show the water adsorption schematics and scanning electron microscope (SEM) image of an advanced adsorbent with micro-pores and exceptionally high surface area. The adsorption characteristics of an adsorbent and adsorbate pair is typically described by an adsorption isotherm. The isotherm is a curve that represents the adsorbed amount as a function of adsorbate vapor pressure at a constant temperature. For water adsorption in particular, the water vapor relative humidity (RH) instead of pressure is more commonly used to plot the isotherm. Figure 5(c) shows the representative isotherms of three main adsorbents used for water adsorption. Zeolite and silica are traditional desiccants that have been used extensively for commercial products and industrial processes. However, their performances are limited by difficulty of releasing adsorbed vapor and low water uptake at low humidity, respectively. In contrast, metal-organic framework (MOF) is a novel class of adsorbents that show superior water adsorption performance at low humidity conditions. Specifically, MOFs exhibit high water uptake and step-shaped adsorption isotherm,[24,34–38] enabling vapor capture and water production at low relative humidity (RH, RH < 40%) and low dew point temperature (< 10 °C).[24,34,37–40] The step-shape of the isotherm also represents the material's sharp transition between adsorption and desorption. This means only a small change in the operating RH (from just above to just below the isotherm step) is needed to fully desorb the adsorbed vapor, effectively reducing the desorption time and energy requirement.
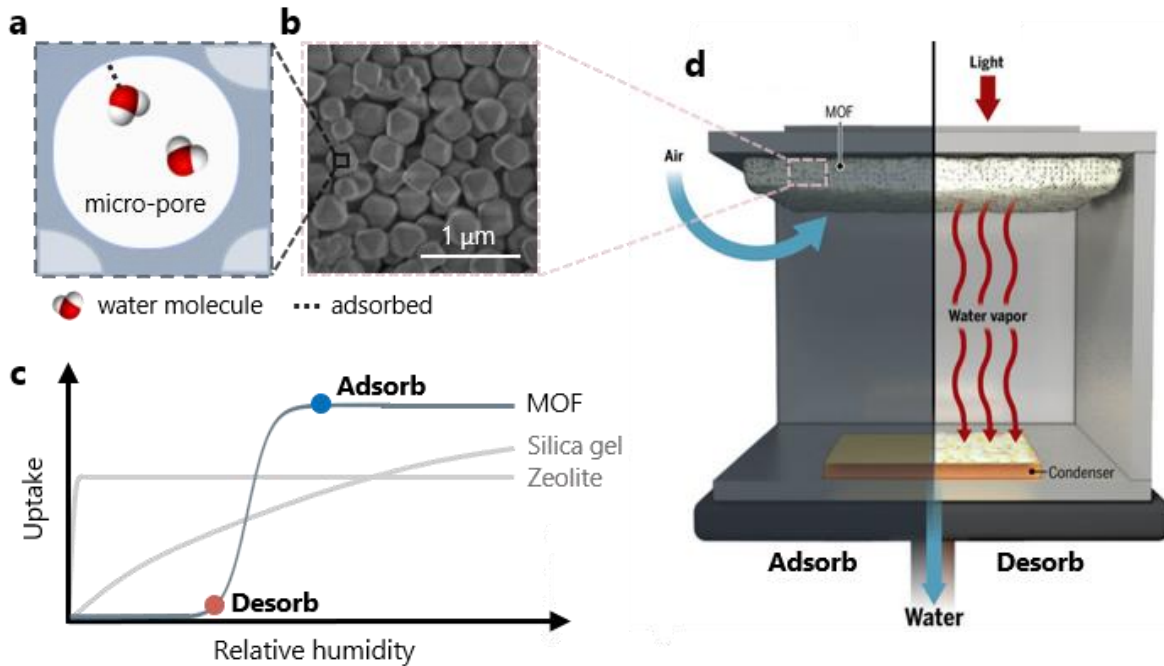
**FIG. 5. Fundamental working principles of adsorbent materials and adsorption-based AWH devices.** (a) A schematic of the adsorption of water molecules in adsorbent micro-pores. (b) SEM image of an advanced adsorbent with micro-pores. (c) Representative isotherms of three main adsorbents used for water adsorption. (d) Illustration of a typical adsorption-based AWH device by Kim *et al.*[41]

A typical adsorption-based AWH device consists of a single adsorbent bed interfaced with a condenser, as shown in Fig. 5(d).[41] The adsorbent bed and condenser are separated by a small air gap in between for vapor transport. The air gap is kept small to reduce vapor transport resistance and losses. During adsorption, the adsorbent bed captures dilute water vapor from the ambient air during adsorption and releases concentrated water vapor upon heating during desorption. The condenser then condenses the desorbed vapor into liquid water by rejecting heat to the ambient.

To further improve the energy efficiency of AWH devices, LaPotin *et al.* proposed a dual-stage device architecture.[34] In the dual-stage configuration, two pairs of adsorbent bed and condenser operate in series. By recycling the condensation heat of the first stage and using it for desorbing the second stage, additional water can be harvested and the overall AWH efficiency can be

increased. Outdoor demonstrations of both single and dual-stage AWH devices reported in recent literature are shown in Fig. 6.[34,41]
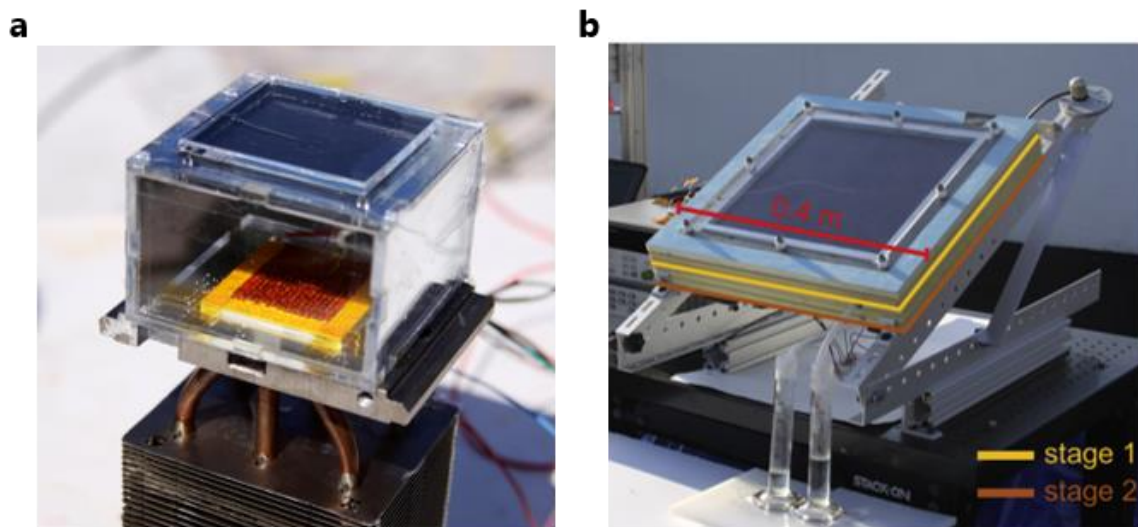


**FIG. 6. Representative adsorption-based AWH devices.** (a) Single-stage device by Kim *et al.*[41] (b) Dual-stage device by LaPotin *et al.*[34]

### 1.2.2.  Knowledge gap and the role of thermodynamics

Recent advances of adsorption-based AWH have focused on adsorbent development, such as metal-organic frameworks (MOFs)[35,36,42–45] and advanced zeolites,[34,46] which enabled vapor capture and water production at low humidity conditions typical for arid climates.[24,34,37–40] Although the characteristics of adsorbents can be largely modified for different operating environments[23,25,47–49] and have a strong impact on device performance,[47] design guidelines on how to engineer adsorbent properties for optimal device-level operation is lacking. Therefore, current designs of AWH devices mainly rely on trial-and-error approaches by testing multiple adsorbents empirically, limiting effective device optimization and scale-up.

Thermodynamic analysis plays a critical role in understanding the fundamental limits of integrating state-of-the-art adsorbents into AWH devices.[50–54] Recent thermodynamic analysis predicted the energy efficiencies of both single and dual-stage AWH devices with select adsorbents[55] and enabled a global-scale assessment of AWH potential.[56] However, a large knowledge gap between adsorbent development and AWH device design remains. On one hand, for a specific adsorbent, it is unclear what the operating conditions should be to achieve optimal

performance of the AWH device. On the other hand, under practical operating constraints (*e.g.*, desorption temperature) and climate conditions, it is unclear what are the most appropriate adsorbent characteristics for optimal AWH performance. More fundamentally, adsorption exhibits a strong temperature-dependence, *i.e.*, the shift of the isotherm hysteresis loop position towards higher relative pressures with increasing temperature. For common adsorbents with negligible hysteresis loops,[38] the adsorption and desorption steps overlap and the overall effect is the right-shift of a single isotherm step position with increasing temperature (we subsequently refer to this effect as the "isotherm-shift"). This isotherm-shift is critical for adsorption but has been largely overlooked in conventional AWH modeling and devices design.

## 1.3.    Thesis objectives and outline

The main objective of this thesis is to present a comprehensive thermodynamic model and set of design guidelines for developing high-performance adsorption-based AWH devices. The thermodynamic model presented here bridges several important knowledge gaps in the fundamental understanding and theoretical modeling of adsorption-based AWH. By capturing the strong coupling between adsorbent characteristics and device operating conditions, we explore the synergistic design of both materials and device for maximum AWH efficiency. Furthermore, we also discuss the design requirements of select device subcomponents toward developing high-performance AWH technology.

In Chapter 1, we discussed the motivation for developing adsorption-base atmospheric water harvesting technologies. We provided an overview of the key drivers, metrics, and impacts of global water scarcity, and discussed the opportunity to address this challenge by harvesting water from the air. We then revisited the working mechanisms and limitations of existing AWH technologies and identified the advantages of adsorption-based technology for arid climates. Lastly, we introduced the significance of thermodynamics, highlighting present knowledge gaps in the design of high-performance adsorption-based AWH devices.

In Chapter 2, we present a generalized thermodynamic model of AWH devices with temperature-dependent adsorption. We consider the ideal thermodynamic cycle and adsorbent properties for adsorption-based AWH and provide key modifications to previous models in literature. Combing theoretical analysis and experimental characterization, we investigate the temperature-dependence of adsorption and the corresponding shift in adsorption isotherm with temperature. Finally, we

derive a thermodynamic model that captures the effect of the isotherm-shift on the device-level performance of adsorption-based AWH.

In Chapter 3, we determine the upper-bound thermal efficiency of adsorption-based AWH devices based on the thermodynamic model, and show significant enhancements as compared to past predictions. We study the effect of both device operating conditions and adsorbent properties on the overall efficiency, providing insights for the synergistic design of materials and device for optimal AWH performance. We also extend the analysis to a dual-stage device configuration and show generality in key results.

In Chapter 4, we discuss the design requirements of atmospheric air delivery and condenser units for developing high-performance adsorption-based AWH devices. For air delivery, we explore three potential candidates based on air flow performance, compactness, and power consumption. Lastly, we estimate the heat transfer and water retention performance of the condenser using baseline theoretical models.

In the final chapter, Chapter 5, we review the key results presented in this thesis and propose opportunities for future work toward high-performance and scalable adsorption-based AWH technologies.

# Chapter 2 Thermodynamic model of AWH devices with temperature-dependent adsorption

In this chapter, we present a generalized thermodynamic model of AWH devices with temperature-dependent adsorption. We consider the ideal thermodynamic cycle and adsorbent properties for adsorption-based AWH and provide key modifications to previous models in literature. Combing theoretical analysis and experimental characterization, we investigate the temperature-dependence of adsorption and the corresponding shift in adsorption isotherm with temperature. Finally, we derive a thermodynamic model that captures the effect of the isotherm-shift on the device-level performance of adsorption-based AWH.

## 2.1    Basic thermodynamic cycle of adsorption-based AWH

Figures 7(a)-1(d) show the operation of a basic single-stage AWH device and the four main steps of the thermodynamic cycle. Starting from a fully adsorbed state, the device first undergoes isosteric heating [Fig. 7(a) and states 1-2 in Fig. 7(e)], where the system temperature increases but no significant desorption happens yet in the adsorbent bed. Due to the initial heating, vapor pressure in the air gap between the condenser and the adsorbent bed also increases. Once the air gap vapor pressure reaches the condenser saturation pressure [state 1' in Fig. 7(e)], however, the pressure becomes pinned and no longer increases during subsequent isosteric heating. Desorption [Fig. 7(b) and states 2-3 in Fig. 7(e)] starts when the system reaches state 2, where the critical desorption pressure of the adsorbent (indicated by the step position of isotherms) reaches the condenser saturation vapor pressure. Upon further heating, desorption continues with higher vapor pressure within the adsorbent bed as the critical desorption pressure of the adsorbent increases with temperature. For a small air gap, the vapor pressure above the adsorption bed remains pinned at the condenser saturation pressure, lower than the adsorbent desorption pressure. As a result, desorption and condensation happen simultaneously, producing liquid water. At the end of desorption, the water content in the adsorbent bed is depleted and the vapor pressure in the adsorbent bed quickly drops and converges to that of the air gap [states 3-3' in Fig. 7(e)]. Finally, the system undergoes isosteric cooling [Fig. 7(c) and states 3'-4 in Fig. 7(e)] before adsorption [Fig. 7(d) and states 4-1 in Fig. 7(e)] occurs again at ambient vapor pressure, and the cycle returns to its initial state. Fig. 7(e) shows the corresponding pressure-temperature (P-T) diagram of the

thermodynamic cycle, which considers equilibrium states of the adsorbent bed only and hence no adsorbent kinetics are involved. The x and y axes show $-1/T$ and $ln(P)$, respectively, with respect to a reference state $(T_0, P_0)$ according to the Clausius-Clapeyron relation. Note that this thermodynamic cycle deviates from the conventional pure-vapor adsorption cycle applied to heat pumps[55,57,58] and refrigerators[55,59] in two folds. First, novel adsorbents with well-defined pores used for AWH have step-shaped isotherms that enable a sharp transition between adsorption and desorption at a critical vapor pressure. Traditional adsorbents with non-uniform pores, on the other hand, exhibit adsorption isotherms with a more gradual increase in the gas uptake over a broad pressure range. Second, AWH devices operate in an air-vapor environment, which includes additional interactions with the ambient air compared with the pure vapor conditions.
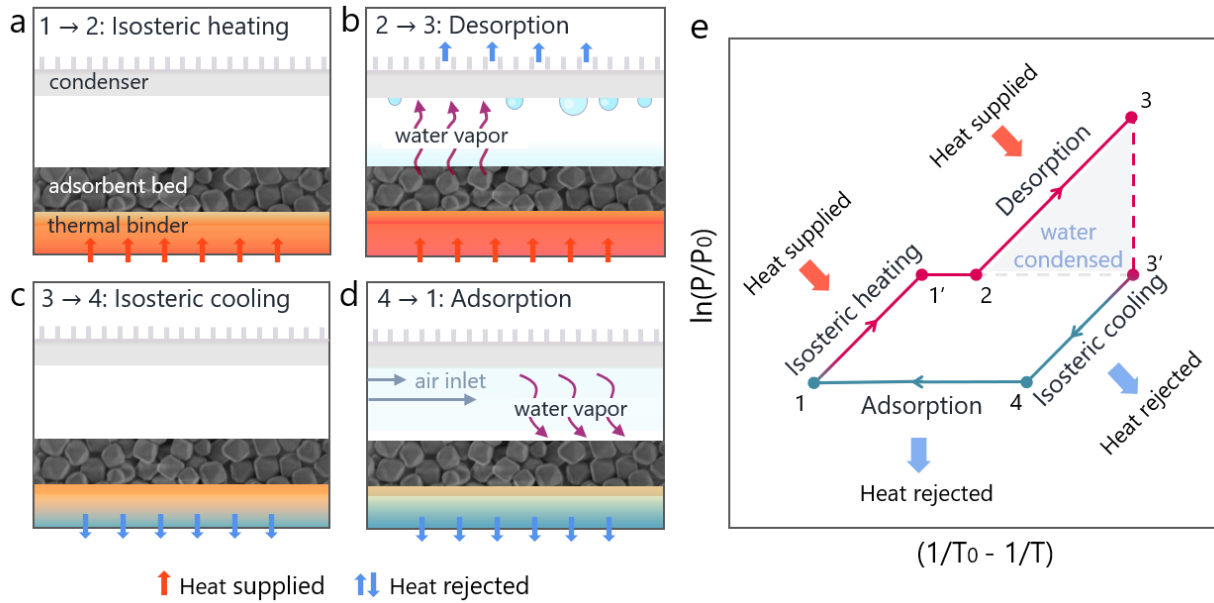


**FIG. 7. General thermodynamic cycle for adsorption-based AWH devices.** Schematics showing the four main steps for the cycle. (a) Isosteric heating. The system temperature and vapor pressure increase because of heating but no significant desorption happens yet in the adsorbent bed. (b) Desorption. The critical desorption condition of the adsorbent bed is reached and significant desorption takes place upon further heating. (c) Isosteric cooling. The system is cooled down but no significant adsorption happens yet in the adsorbent bed. (d) Adsorption. The temperature and vapor pressure of the adsorbent bed are decreased sufficiently and significant adsorption happens at ambient vapor pressure. (e) Thermodynamic cycle on a pressure-

22

temperature (P-T) diagram showing key physical states. The x and y axes show $-1/T$ and $ln(P)$, respectively, with respect to a reference state $(T_0, P_0)$ according to the Clausius-Clapeyron relation.

## 2.2    Ideal adsorption isotherm

For the thermodynamic framework proposed in this work, we assume an ideal adsorption isotherm shape that gives the maximum device thermal efficiency (theoretical limit) while satisfying the general thermodynamic cycle of an adsorption-based system shown in Fig. 7. Instead of assuming an ideal-step isotherm profile as in the case of the literature model[55], we assume a small gradient in the isotherm [step a in Fig. 8(a)] before and after its major step [step d in Fig. 8(a)] to enable slight water vapor exchange between the adsorbent surface and the air gap during isosteric heating and cooling. The effect is that the vapor pressure in the air gap changes while the adsorbent uptake remains approximately constant during the isosteric steps, which is suggested but not well explained in past models on conventional adsorption systems.[55,57,60,61]

Fig. 8(b) shows the locations of key states on the idealized adsorption isotherm during a thermodynamic cycle of AWH. In this work, we define 'desorption' as the significant desorption that occurs during step 2-3 only of the isotherm. The uptake changes during 1-2 and 3-4 are small, if not negligible, based on further considerations of the device configuration. Further, in this work, we assume the water accommodation capacity of the adsorbent bed $n_{w,ads}$ is much larger than that of the air gap $n_{w,air}$ [Fig. 8(c)]. As a result, vapor pressure in the air gap during the isosteric heating is dominated by the material response of the adsorbent bed, *i.e.*, the increase in the air gap vapor pressure follows the desorption vapor pressure [right-shift of isotherm step position, Fig. 8(c)]. Accordingly, in the pressure-temperature (P-T) diagram [Fig. 7(e)], the slope of step 1-1' on the thermodynamic diagram is the same as the slope of step 2-3, because both steps are determined by the isotherm-shift with temperature.
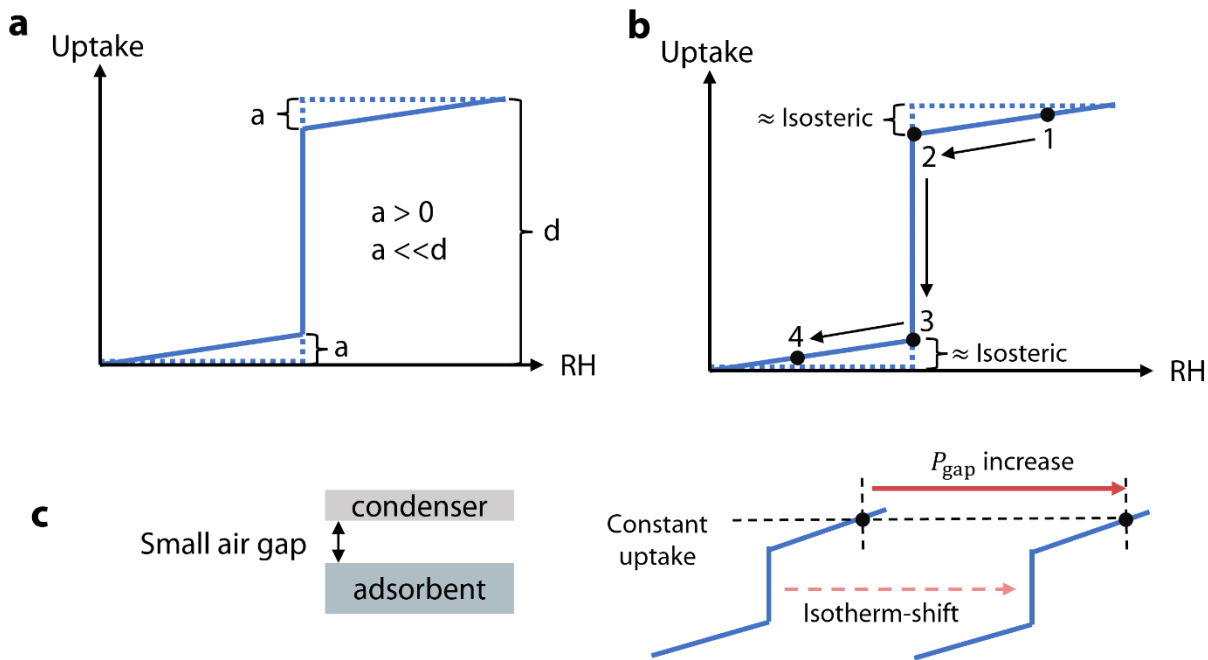
**FIG. 8. Ideal adsorption isotherm profile for thermodynamic modeling.** (a) An ideal step-shaped adsorption isotherm for MOF, which is a near ideal step function that satisfies the geometric criteria specified on the diagram. (b) Location of key states on the idealized adsorption isotherm during a thermodynamic cycle for AWH. (c) Assuming that the air gap is small and the adsorbent bed acts as a water vapor reservoir, the adsorbent uptake remains approximately constant (isosteric) and $P_{gap}$ increase follows the isotherm-shift during initial heating.

We note that the use of advanced adsorbents for AWH and the corresponding assumption of an ideal step-shaped isotherm, as detailed in this section, deviate from conventional pure-vapor adsorption systems like heat pumps[55,57,58] and refrigerators[55,59]. The step-shaped isotherms of novel adsorbents with well-defined pores used for AWH enable a sharp transition between adsorption and desorption at a critical vapor pressure. Traditional adsorbents with non-uniform pores, on the other hand, exhibit adsorption isotherms with a more gradual increase in the gas uptake over a broad pressure range. Furthermore, AWH devices operate in an air-vapor environment, which includes additional interactions with the ambient air compared with the pure vapor conditions. The combination of differences in isotherm type and working fluid leads to differences between the

thermodynamic cycle of AWH (shown in this work) and those of conventional adsorption-based systems.

## 2.3. Temperature dependence of adsorption

### 2.3.1. Experimental characterizations

It has been widely reported in literature that the $P_{des}$ of adsorbents, such as MOFs and zeolites, exhibits a significant temperature dependence.[24,34,62–64] To illustrate the effect of the isotherm-shift, we used MOF-303 as an example material because it has been recently used for AWH and shown great stability and cyclability.[38,55,65] MOF-303 has a formula of [Al(OH)(HPDC); HPDC, 1H-pyrazole-3,5-dicarboxylate] and it features 1D channel structure of hydrophilic pores with 0.6 nm in diameter.[65] We purchased commercially available MOF-303 from Beijing Beike 2D materials Co., Ltd., and inspected the crystal quality using scanning electron microscopy (SEM). Figure 9. below shows an example SEM image of our MOF-303 sample taken using the Zeiss Gemini SEM at MIT Materials Research Science and Engineering Center (MRSEC). The setting parameters used for obtaining the image in Fig. 9(a) are summarized in Table 1.
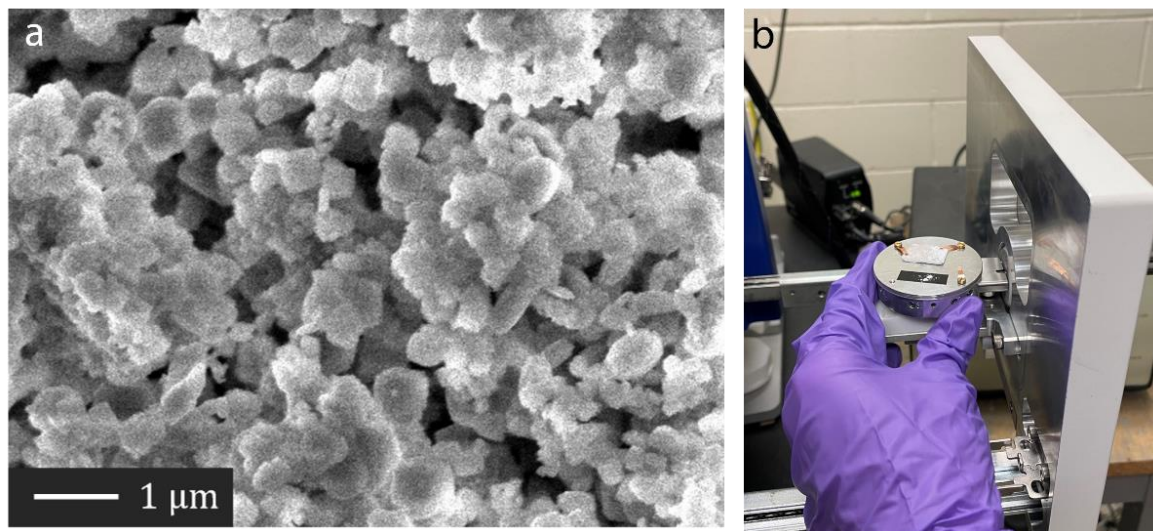


**FIG. 9. SEM imaging of MOF-303 sample (Beijing Beike 2D materials Co., Ltd.) used for adsorption isotherm characterizations.** (a) SEM image showing MOF-303 crystals. (b) Sample mounting on the Zeiss Gemini SEM at MIT CMSE used for the imaging.

**TABLE. 1. Zeiss Gemini SEM settings used for the image shown in Fig. 9(a).**

| Setting parameter | Value |
|---|---|
| EHT | 5.00 kV |
| Mag | 6.84 K X |
| Signal A | InLens |
| I Probe | 100 pA |
| WD | 4.0 mm |
| Column Mode | High Resolution |

We then characterized the adsorption isotherm of MOF-303 using dynamic vapor sorption (DVS), over a range of temperatures. The instrument we used was DVS Vacuum by Surface Measurement Systems Ltd. Figure 10 below shows a representative plot of a successful run at 25°C, showing the target step changes in the adsorbent and corresponding changes in sample mass over time during the experiment.
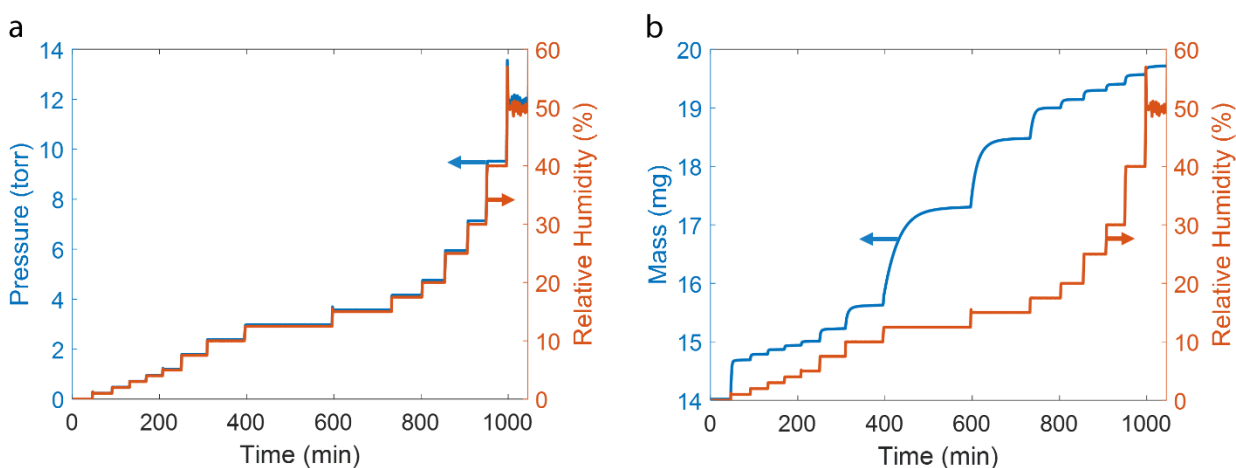


**FIG. 10. Sample DVS raw data of MOF-303 isotherm characterization at 25°C.** (a) Step changes in the chamber vapor pressure (blue line, left axis) and corresponding relative humidity

experienced by the adsorbent (orange line, right axis) as a function of time during adsorption. (b) Changes in the adsorbent mass (blue line, left axis) due to changes in the relative humidityexperienced by the adsorbent (orange line, right axis) as a function of time during adsorption.

To confirm that the hysteresis loop of MOF-303 is closed [Fig. 11(b)],[38] *i.e.*, the adsorption and desorption isotherms overlap, we also measured the desorption isotherm of MOF-303 initially. Fig. 11(a) shows the DVS measurements of both the adsorption and desorption steps of MOF-303 at 25°C.
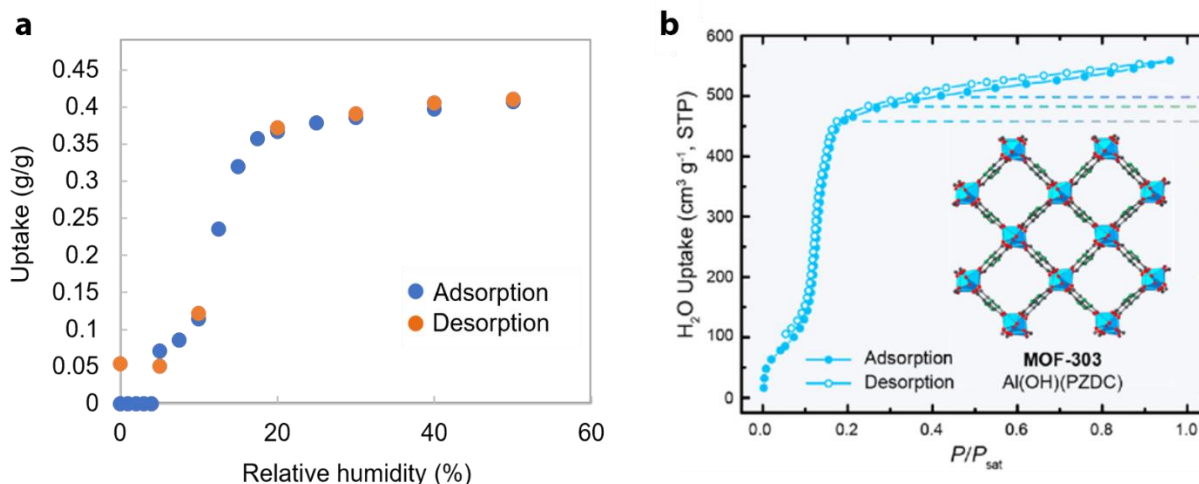


**FIG. 11. Experimental observations of negligible hystresis in MOF-303.** (a) DVS measurements of the MOF-303 adsorption and desorption isotherms at 25°C. (b) Literature data on the MOF-303 adsorption and desorption isotherms at 30 °C.[38] (Inset: structure of MOF-303)

### 2.3.2. Non-linear regression

To obtain a continuous isotherm and extract key physical parameters, we performed non-linear regression of the experimental isotherm data measured using the DVS. Rahman *et al.*[62] proposed the following Li-Jensen-May-Yang (LJMY)-Langmuir model for the fitting and parameter extraction of step-shaped MOF isotherm,

$$Q = Q_\mathrm{m} \frac{KP}{1 + KP} + \frac{Q_\mathrm{step}}{2}\left[1 + erf\left(\frac{P - P_\mathrm{des}}{\sqrt{2}\sigma}\right)\right] \tag{1}$$

where $Q$ is the adsorbent equilibrium uptake and p is the adsorbate vapor pressure.

The LJMY-Langmuir model contains five fitting parameters that each has an associated physical meaning, as summarized in Table 2. The parameter $P_\mathrm{des}$ captures the critical desorption vapor pressure (corresponding to the step position) of the adsorbent at the experimented temperature, and therefore, the change in $P_\mathrm{des}$ with the desorption temperature is key to characterizing the isotherm shifting with temperature. The best fit values of $P_{des}$ determined from the nonlinear regression using the LJMY-Langmuir model and the associated standard errors of fitting are summarized in Table 3. The low standard error (SE) and high R-squared values indicate a very good fit between the experimental data and the LJMY-Langmuir regression model.

**TABLE 2. LJMY-Langmuir model fitting parameters and their physical meanings**

| Parameter | Physical meaning |
|---|---|
| $Q_\mathrm{m}$ | Langmuir limiting uptake |
| $K$ | Initial slope |
| $Q_\mathrm{step}$ | LJMY limiting uptake |
| $P_\mathrm{des}$ | Transition vapor pressure |
| $\sigma$ | Error function shape factor |

**TABLE 3. Best fit values of $P_\mathrm{des}$ determined from the nonlinear regression.**

| Temperature (°C) | $P_\mathrm{des}$ (kPa) | Standard error of $P_\mathrm{des}$ | R-squared value |
|---|---|---|---|
| 25 | 0.39 | 0.005 | 0.999 |
| 50 | 2.04 | 0.018 | 0.999 |
| 80 | 13.28 | 0.172 | 0.999 |

### 2.3.3. Adsorption isotherm-shift with temperature

Figure 12(a) shows the experimentally measured and fitted isotherms of water vapor adsorption in MOF-303 at 25°C, 50°C and 80°C. A clear increase of the critical desorption pressure (indicated by the step position of isotherms) with temperature can be seen. To quantify this isotherm-shift, we considered the thermodynamics of phase equilibrium between the adsorbed and gaseous states of water, which can be described by the Clausius-Clapeyron relation,[62]

$$\ln\left(\frac{P_{des}}{P_{des,0}}\right) = \frac{h_{ad}}{R}\left(\frac{1}{T_0} - \frac{1}{T}\right) \tag{2}$$

where $P_{des,0}$ is the critical desorption pressure at a reference temperature $T_0$ and $R$ is the universal gas constant.
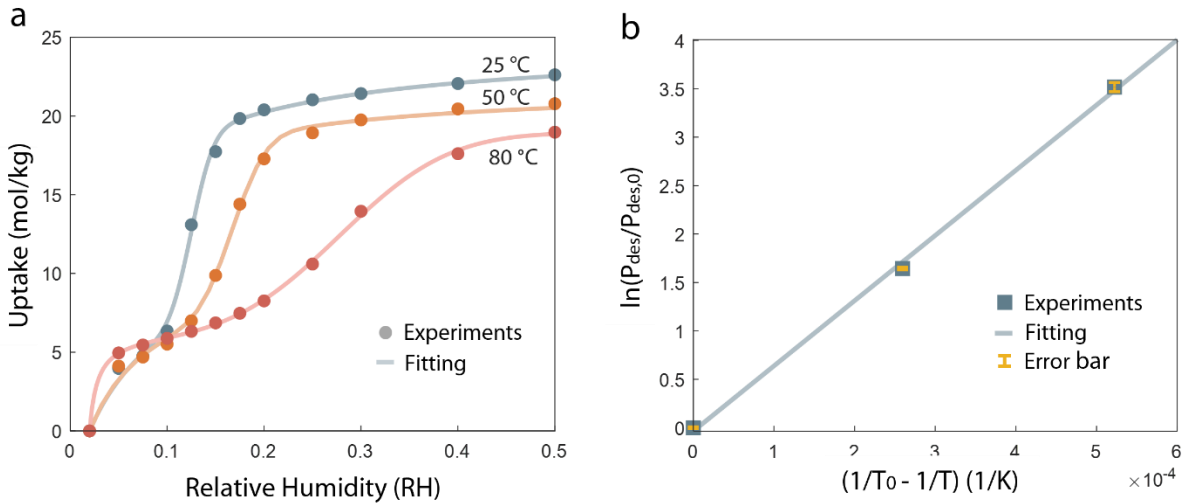


**FIG. 12. Isotherm-shift of MOF-303 with temperature.** (a) Water adsorption isotherms of MOF-303 at 25°C (blue), 50°C (orange) and 80°C (red). The solid circles are adsorption isotherms characterized by DVS. The solid curves are nonlinear fitting of adsorption isotherms using the Li-Jensen-May-Yang (LJMY)-Langmuir model.[62] (b) Isotherm step positions as a function of temperature. The square symbols are isotherm step positions determined from experimental characterizations. The solid lines are linear fits showing that the temperature dependence of the isotherm step follows the Clausius-Clapeyron relation.

We validated Eq. (2) by plotting the transformed critical desorption pressure, $\ln(P_{des}/P_{des,0})$, as a function of transformed temperature, $(1/T_0 - 1/T)$, as shown in Fig. 12(b). Due to this transformation of variables, the error bars associated with the data points shown in Fig. 12(b) represent the propagated error of $y = \ln(P_{des}/P_{des,0}) = \ln(P_{des}) - \ln(P_{des,0})$. This can be calculated from the standard errors of fitted $P_{des}$ according to the uncertainty propagation principle,[66]

$$\delta y = \sqrt{\left(\frac{1}{P_{des}} \times \delta P_{des}\right)^2 + \left(\frac{1}{P_{des,0}} \times \delta P_{des,0}\right)^2} \tag{3}$$

where $\delta P_{des}$ and $P_{des,0}$ are the standard errors of $P_{des}(T)$ and $P_{des}(T_0)$ associated with the nonlinear regression of adsorption isotherms, as summarized in Table 3. In this work, $T_0 = 25\ °C$. The propagated errors of $ln(P_{des}/P_{des,0})$ calculated using Eq. (3) are reflected as y-axis error bars on the data points in Fig. 12(b).

A clear linear dependence between $\ln(P_{des}/P_{des,0})$ and $(1/T_0 - 1/T)$ is shown in Fig. 12(b), demonstrating that the isotherm-shift with temperature is well-captured by Eq. (2). As required by the Clausius-Clapeyron equation, the molar volume of the adsorbed phase must be negligible, and the vapor phase demonstrate ideal gas behavior,[67,68] a valid assumption at the low relative pressures used for fitting (see supplementary material Section 6 for details of variable transformation and error propagation calculations). In addition, we estimated the adsorption enthalpy of MOF-303 from the linear slope based on Eq. 2 ($\approx$ 3000 kJ/kg), which shows great agreement with the literature reported value ($\approx$ 2900 kJ/kg).[38]

## 2.4. Model derivation incorporating the temperature dependence of adsorption

A key aspect of the thermodynamic modeling of AWH is to capture the amount of energy needed to release the adsorbed water in the adsorbent bed as vapor, allowing for subsequent condensation and liquid water production. The total amount of energy input $Q_{reg}$ per mass of produced water $m_w$ in a cycle is defined as the specific regeneration energy, $Q_{reg}/m_w$. We considered the AWH device to be passively cooled by ambient air, so no additional energy is required for heat rejection, which is consistent with the practical operation of representative AWH devices.[37,55] Considering the ideal step-shaped isotherm defined in Section 2.3.2, the specific regeneration energy can be obtained from the First Law of Thermodynamics,[55]

$$\frac{Q_{reg}}{m_w} = \left[\frac{1}{w}\left(c_{p,ad} + c_{p,bi}\right) + c_{p,w}\right](T_3 - T_1) + \frac{1}{\omega_3 - \omega_2}\left(c_{p,air} + \omega_2 c_{p,v}\right)(T_3 - T_{cond}) + h_{ad} \qquad (4)$$

where $w$, $c_p$, $T$ and $h_{ad}$ are the adsorbent water uptake, specific heat capacity, temperature, and specific adsorption enthalpy, respectively. $c_{p,ad}$, $c_{p,bi}$, $c_{p,w}$, $c_{p,air}$ and $c_{p,v}$ are the specific heat capacities of adsorbent and thermal binder, water, dry air, and vapor, respectively. $\omega_2$ and $\omega_3$ are the humidity ratios at the surface of the adsorbent bed in states 2 and 3, respectively. Since the vapor pressure within the adsorption bed is dictated by the critical desorption pressure of adsorbents $P_{des}$, the humidity ratio $\omega$ is thus given by,

$$\omega = 0.62198\frac{P_{des}}{P_a} \qquad (5)$$

where $P_a$ is the dry air pressure. Eq. (4) has a clear physical meaning, where the three terms on the right-hand side represent the thermal energies for sensible heating of solids, air-vapor mixture, and enthalpy of adsorption (desorption), respectively.

Equation 4 was modified from previous theory based on conservation laws and scaling analysis. The specific regeneration energy equation proposed in previous model[55],

$$\frac{Q_{reg}}{m_w} = \left[\frac{1}{w}\left(c_{p,ad} + c_{p,bi}\right) + c_{p,w}\right](T_3 - T_1) + \frac{1}{\omega_a - \omega_b}\left(c_{p,air} + \omega_b c_{p,v}\right)(T_3 - T_{cond}) \\ + h_{ad} \qquad (6)$$

where $w$, $c_p$, $T$ and $h_{ad}$ are the adsorbent water uptake, specific heat capacity, temperature, and specific adsorption enthalpy, respectively. $c_{p,ad}$, $c_{p,bi}$, $c_{p,w}$, $c_{p,air}$ and $c_{p,v}$ are the specific heat capacities of adsorbent and thermal binder, water, dry air, and vapor, respectively. $\omega_b$ is the humidity ratio at the surface of the adsorbent bed in states 2, $\omega_2$, which equals the humidity ratio in the air gap at the saturation vapor pressure of the condenser. $\omega_a$ is an effective humidity ratio evaluated between states 2 and 3 calculated as,

$$\omega_a = \frac{\int_{T_2}^{T_3} 0.62198 \frac{P_v(T)}{P_a} \, dT}{T_3 - T_2} \tag{7}$$

where $P_v$ is the desorption vapor pressure and $P_a$ is the dry air pressure.

A physical interpretation of this formulation is that desorption happens gradually between states 2 and 3, and therefore the desorbed water vapor leaves the adsorbent bed surface at vapor pressures ranging from $P_{des}(T_2)$ to $P_{des}(T_3)$ during the heating from $T_2$ to $T_3$. However, the first term of the equation accounts for the sensible heating of all of the adsorbed water (full uptake) in the adsorbent bed all the way from $T_1$ to $T_3$, which implies the amount of adsorbed water in the adsorbent bed does not change from $T_1$ to $T_3$. This is a contradiction to the assumption about the desorbed vapor state described previously and violates the conservation of mass of water. Specifically, the total mass of water vapor that is desorbed and remaining adsorbed must stay constant (matches full uptake) at any time during desorption. As a result, there cannot be gradual water vapor desorption from $T_2$ to $T_3$ when the adsorbent uptake is assumed to be constant from $T_1$ to $T_3$. To resolve this contradiction, we re-define $\omega_a$ to be the humidity ratio at state 3, $\omega_3$, in this work. The physical implication of the change is that we now must assume that the adsorbent heats up much faster than it desorbs, and therefore, most of the adsorbent water is desorbed at state 3. This assumption can be justified with a simple scaling analysis. The time scale for heating up the adsorbent is shorter than that of desorption when the thermal diffusivity ($\alpha$) is significantly higher than the mass diffusivity ($D$) of the material, $i.e.$, the Lewis number $\left(Le = \frac{\alpha}{D}\right)$ is high ($\sim 10$) during simultaneous heat and mass transfer, which applies to common MOFs. These updated assumptions yield Eq. (4).

To calculate $\omega_3$ and $\omega_2$ using the equations shown above, the partial pressure of dry air in the air gap and adsorbent bed surface needs to be evaluated at the respective states. We note that for this

purpose, it is reasonable to either assume the total pressure is constant (open system) or changes from the ambient state according to the ideal gas law upon heating (closed system), depending on the device configuration. In this work we assume that the total pressure is constant and at 1 atm (101 kPa). This assumption is appropriate because we model the device as an internal-circulation system analogous to an open system, following the original model proposed by Kim $et$ $al.$[55] Therefore, the dry air pressure ($P_a$) and water vapor pressure ($P_v$) can be related as,

$$P_a = P_{atm} - P_v \qquad (8)$$

and the humidity ratio can be generally written as,

$$\omega = 0.62198 \frac{P_v}{P_a} = 0.62198 \frac{P_v}{P_{atm} - P_v}. \qquad (9)$$

Isotherm-shift studies conducted previously[62] and in this work indicate that the desorption vapor pressure of the adsorbent is a function of temperature described by the Clausius-Clapeyron effect. We can therefore write $\omega_3$ from Eq. (4) in the following form that takes the isotherm-shift into account.

$$\omega_3 = \omega(T_3) = 0.62198 \frac{P_v}{P_a} \qquad (10.a)$$

$$= 0.62198 \frac{P_{des,0} \times \exp\left[\frac{h_{ad}}{R}\left(\frac{1}{T_0} - \frac{1}{T_3}\right)\right]}{P_a} \qquad (10.b)$$

$$= 0.62198 \frac{P_{des,0} \times \exp\left[\frac{h_{ad}}{R}\left(\frac{1}{T_0} - \frac{1}{T_3}\right)\right]}{P_{atm} - P_{des,0} \times \exp\left[\frac{h_{ad}}{R}\left(\frac{1}{T_0} - \frac{1}{T_3}\right)\right]} \qquad (10.c)$$

where $h_{ad}$, $R$ and $P_{atm}$ are the specific adsorption enthalpy, the universal gas constant, and the atmospheric pressure, respectively. $T_0$ is a reference temperature in K and $P_{des,0}$ is the corresponding critical desorption vapor pressure (step position of isotherm) of the adsorbent at $T_0$.

Knowing the condenser temperature and the corresponding condenser (and air gap) saturation pressure, the humidity ratio at state 2 can be obtained directly from the definition of humidity ratio,

$$\omega_2 = 0.62198 \frac{P_v}{P_a} = 0.62198 \frac{P_{sat}(T_{cond})}{P_{atm} - P_{sat}(T_{cond})}. \tag{11}$$

The final expression for the specific regeneration energy incorporating the isotherm-shift is then,

$$
\begin{aligned}
\frac{Q_{reg}}{m_w} &= \left[ \frac{1}{w} \left( c_{p,ad} + c_{p,bi} \right) + c_{p,w} \right] (T_3 - T_1) \\
&+ \frac{1}{0.62198 \dfrac{P_{des,0} \times \exp\left[ \frac{h_{ad}}{R} \left( \frac{1}{T_0} - \frac{1}{T_3} \right) \right]}{P_{atm} - P_{des,0} \times \exp\left[ \frac{h_{ad}}{R} \left( \frac{1}{T_0} - \frac{1}{T_3} \right) \right]} - 0.62198 \dfrac{P_{sat}(T_{cond})}{P_{atm} - P_{sat}(T_{cond})}} \\
&\quad \left( c_{p,air} + 0.62198 \frac{P_{sat}(T_{cond})}{P_{atm} - P_{sat}(T_{cond})} c_{p,v} \right) (T_3 - T_{cond}) + h_{ad}
\end{aligned}
\tag{12}
$$

where $w$, $c_p$, $T$ and $h_{ad}$ are the adsorbent water uptake, specific heat capacity, temperature, and specific adsorption enthalpy, respectively. $c_{p,ad}$, $c_{p,bi}$, $c_{p,w}$, $c_{p,air}$ and $c_{p,v}$ are the specific heat capacities of the adsorbent and thermal binder, water, dry air, and vapor, respectively. $h_{ad}$, $R$ and $P_{atm}$ are the specific adsorption enthalpy, the universal gas constant, and the atmospheric pressure, respectively. $T_0$ is a reference temperature in K and $P_{des,0}$ is the corresponding critical desorption vapor pressure (step position of isotherm) of the adsorbent at $T_0$. $T_{cond}$ is the condenser temperature, and $P_{sat}(T_{cond})$ is the saturation vapor pressure evaluated at $T_{cond}$. Note that we treated $w$ and $h_{ad}$ as constants because adsorption occurs at ambient temperature and $h_{ad}$ weakly depends on temperature.

The device-level thermal efficiency $\eta_t$ is defined as the ratio of water vaporization enthalpy $h_{fg}$ and specific regeneration energy,[55]

$$\eta_t = \frac{m_w h_{fg}}{Q_{reg}}. \tag{13}$$

Equation 12 is a key result of the present framework, as it explicitly shows the impacts of material adsorption characteristics (e.g., $w$, $P_{\text{des}}$, and $h_{\text{ad}}$) on the thermodynamic performance of the device due to operating conditions (e.g., $T_1$, $T_3$, and $T_{\text{cond}}$. The combination of Eqs. 12 and 13 enabled subsequent analysis on the optimization of device configuration and adsorbent properties for maximizing AWH efficiency.

# Chapter 3: Upper-bound thermal efficiency of adsorption-based AWH

## 3.1.  Impact of device operating conditions

Fig. 13(a) shows the device-level thermal efficiency $\eta_t$ as a function of desorption temperature $T_{des}$ predicted by our model. We show the significant impact of considering the isotherm-shift on the AWH device performance, where a much higher thermal efficiency exceeding the conventional limits is possible. Owing to the isotherm-shift, a lower $T_{des}$ [≈ 50 °C, grey-dashed line in Fig. 13(a)] and higher $\eta_t$ were predicted [orange-solid line in Fig. 13(a)], as compared with the previous theory assuming a fixed adsorption isotherm [≈ 70 °C $T_{des}$, grey-solid line in Fig. 13a].[55] For example, when $T_{des}$ was 100 °C, $\eta_t$ reached 0.55 in our model, which is more than 50% higher than the prediction neglecting the isotherm-shift ($\eta_t$ ≈ 0.35). More interestingly, we show that $\eta_t$ first increased with $T_{des}$ [regime 1 in Fig. 13(a)] and then decreased [regime 2 in Fig. 13(a)], leading to a peak thermal efficiency of 0.58 at ≈ 135 °C [green point in Fig. 13(a)]. When $T_{des}$ became sufficiently high (> 250 °C), our modeling results gradually converged with the previous theory [regime 3 in Fig. 13(a)]. Note that since desorption is fundamentally different from liquid-vapor phase change, the desorption temperature is not pinned by the saturation temperature of water (100 °C) at ambient pressure. However, the condenser temperature $T_{cond}$ (25 °C in the above analysis) must be lower than the saturation temperature to enable vapor condensation.
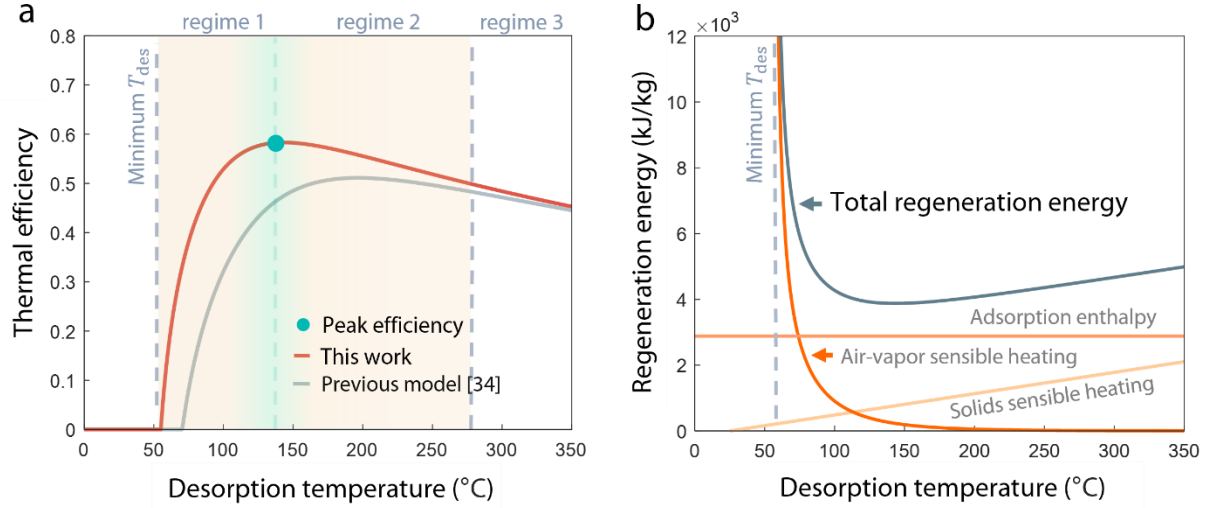
**FIG. 13. Thermal efficiency and regeneration energy of single-stage device from thermodynamic analysis.** (a) Thermal efficiency ($\eta_t$) of single-stage AWE device as a function of desorption temperature ($T_{des}$) by considering the temperature-dependent isotherms. Orange curve shows the improved thermodynamic model presented in this work. Grey curve shows the previous model without taking the isotherm-shift into account[55]. Due to the inclusion of the isotherm-shift, our thermodynamic model predicts higher thermal efficiency than the previous model at the same operating conditions. Three regimes of thermal efficiency with distinct temperature dependences were also observed. Regime 1: $\eta_t$ increases with $T_{des}$, until a maximum $\eta_t$ is achieved. Regime 2: $\eta_t$ begins to drop as $T_{des}$ further increases. Regime 3: $\eta_t$ keeps decreasing with $T_{des}$ and converges with the previous model. (b) Total specific energy (grey curve) required to regenerate all adsorbed vapor as a function of desorption temperature. The total specific energy consists of the sensible heating of solid and air-vapor, as well as the adsorption enthalpy of vapor, which are plotted in orange.

To further elucidate the underlying mechanisms of thermal efficiency due to desorption temperature, we investigated the contributions of the three components of the regeneration energy to $\eta_t$ (Eq. (4)). Fig. 13(b) shows the regeneration energy due to solid sensible heating, air-vapor sensible heating, and adsorption enthalpy as a function of desorption temperature. The regeneration energy for solid sensible heating monotonically increased with $T_{des}$. However, the regeneration energy for the air-vapor sensible heating showed a decreasing trend due to the isotherm-shift. Higher $T_{des}$ induces larger desorption pressure $P_{des}$ [Eq. (3) and Fig. 12], which

leads to a higher humidity ratio $\omega$ (Eq. (2)) and a decrease in air-vapor sensible heating per mass of water harvested [Eq. (4) and Fig. 13(b)]. The opposite trends of the solid and air-vapor sensible heating with desorption temperature results in a minimum total regeneration energy at $\approx$ 135 °C [grey-solid line in Fig. 13(b)], corresponding to the peak thermal efficiency in Fig. 13(a). Since the impact of isotherm-shift is mainly on the air-vapor sensible heating, when $T_{\text{des}}$ is sufficiently high (> 250 °C), the air-vapor sensible heating approaches zero. Therefore, our modeling results finally match the previous predictions in the high-temperature regime [regime 3 in Fig. 13(a)], where the effect of air becomes negligible, and all models approach the pure-vapor case.

## 3.2. Impact of material adsorption enthalpy

In addition to optimizing the desorption temperature for a given adsorbent such as MOF-303, our thermodynamic framework can guide the design of key adsorption characteristics of a material to further improve AWH device performance. We first focused on studying the adsorption enthalpy $h_{\text{ad}}$ because it is expected to have dominant effects on the device performance based on Eq. (4). Fig. 14(a) shows the device-level thermal efficiency $\eta_{\text{t}}$ as a function of $h_{\text{ad}}$ at representative desorption temperatures ranging from 50 °C to 130 °C. In general, $\eta_{\text{t}}$ first increases with $h_{\text{ad}}$ and then decreases, leading to an optimal $h_{\text{ad}}$ for each specific operating temperature. We also plot the adsorption enthalpy of MOF-303 and MOF-801 [grey band in Fig. 14(a)] as a reference to show their current performance as compared with the optimal $h_{\text{ad}}$ at difference temperatures [grey-dashed line in Fig. 14(a)]. In contrast to the conventional understanding, our modeling results suggest that pursuing lower adsorption enthalpy is not always more desirable. For example, considering a desorption temperature of 80 °C, $\eta_{\text{t}}$ can increase from 0.34 to 0.46 when increasing $h_{\text{ad}}$ from 2500 kJ/kg to 3500 kJ/kg. The benefits of increasing desorption temperature become even more significant at lower operating temperatures [Fig. 14(a)]. This result is because for the device-level operation, the total energy consumed for vapor regeneration is not only determined by desorption but also sensible heating, which is related to $h_{\text{ad}}$ as well. Fig. 14(b) shows the regeneration energy due to solid sensible heating, air-vapor sensible heating, and adsorption enthalpy as a function of adsorption enthalpy at $T_{\text{des}}$ = 80 °C. Despite the increase of adsorption enthalpy, air-vapor sensible heating monotonically decreases with $h_{\text{ad}}$, because a higher $h_{\text{ad}}$ indicates a stronger isotherm-shift (Eq. (2), which leads to a larger critical desorption pressure and lower regeneration energy for air-vapor sensible heating (Eqs. (4) and (5)). In particular, at low

$h_{ad}$, the regeneration energy for air-vapor sensible heating is more significant than that for desorption [Fig. 14(b)], which explains why reducing $h_{ad}$ is not always beneficial. Due to the opposing trends of adsorption enthalpy and air-vapor sensible heating, there is an optimal $h_{ad}$, corresponding to the minimum total regeneration energy [Fig. 14(b)] and peak thermal efficiency [Fig. 14(a)]. From a thermodynamic viewpoint, our results suggest a large opportunity space to further engineer adsorption enthalpy of the material based on the operating temperature of AWH devices.
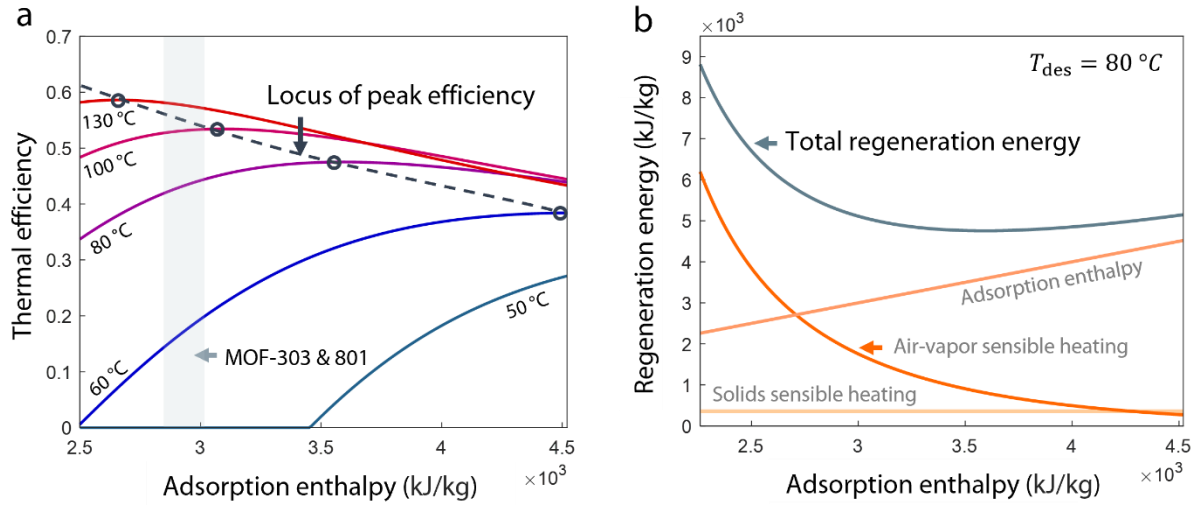


**FIG 14. Effect of adsorption enthalpy on single-stage device thermal efficiency.** (a) Thermal efficiency ($\eta_t$) of a single-stage AWH device as a function of specific adsorption enthalpy ($h_{ad}$) at different desorption temperatures from 50 °C to 130 °C. $\eta_t$ first increases with $h_{ad}$ and then decreases, resulting in a peak corresponding to the optimal thermal efficiency. $\eta_t$ at different temperatures converge to the same linear dependence at high $h_{ad}$. Dashed curve: peak values of $\eta_t$ at difference temperatures. Grey band represents the adsorption enthalpy of MOF-303 and MOF-801 from literature.[33] (b) Total specific energy (gray curve) required to regenerate all adsorbed vapor as a function of specific adsorption enthalpy at 80 °C. The total specific energy consists of the sensible heating of the solid and air-vapor, as well as the adsorption enthalpy of vapor, which are plotted in orange.

## 3.3. Extension to dual-stage devices

To further extend the applicability of our thermodynamic model, we next predicted the thermodynamic limits of a dual-stage AWH device[34] to enable higher efficiency. Fig. 15 shows the dual-stage concept proposed by LaPotin *et al.*,[34] and the associated key operating temperatures. The energy recycled at the condenser of the first stage can be calculated as,

$$\frac{Q_{\text{cond}}}{m_{\text{w}}} = \frac{1}{\omega_3 - \omega_2}\left(c_{\text{p,air}} + \omega_3 c_{\text{p,v}}\right)(T_{\text{des}} - T_{\text{cond}}) + h_{\text{fg}} \qquad (14)$$

where $c_{\text{p,air}}$ and $c_{\text{p,v}}$ are the specific heat capacities of dry air and vapor, respectively. $h_{\text{fg}}$ is specific latent heat of vaporization (condensation). $T_{\text{des}}$ and $T_{\text{cond}}$ are the desorption temperature and condenser temperature, respectively. $\omega_2$ and $\omega_3$ are the humidity ratios at the surface of the adsorbent bed in states 2 and 3, which can be calculated from Eqs. (10.c) and (11), respectively.
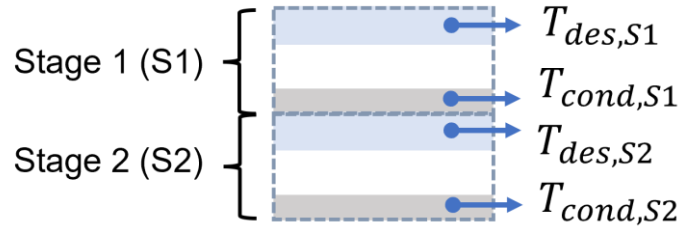


**FIG. 15. Schematics of dual-stage AWH device configuration and key temperatures.** Blue box represents adsorbent beds and gray box represents condenser.

The mass ratio of water harvested from the first and second stage can be found using,

$$\frac{m_{\text{w,2}}}{m_{\text{w}}} = \frac{Q_{\text{cond,}S1}(T_{\text{des,}S1}, T_{\text{cond,}S1})}{m_{\text{w}}} \bigg/ \frac{Q_{\text{reg,}S2}(T_{\text{des,}S2}, T_{\text{cond,}S2})}{m_{\text{w,2}}} \qquad (15)$$

where $m_{\text{w}}$ and $m_{\text{w,2}}$ are the mass of water harvested in the first and second stage, respectively. Subscripts $S1$ and $S2$ represent the first and second stage of the dual-stage system, respectively.

The dual-stage thermal efficiency can then be calculated as,

$$\eta_{t,DS} = \left(1 + \frac{m_{w,2}}{m_w}\right)\eta_t \tag{16}$$

where $\eta_t$ is the thermal efficiency of the first stage operated at $T_{des,S1}$ and $T_{cond,S1}$.

We note that the second stage of a dual-stage device is activated when there is sufficient temperature gradient between its adsorbent bed and condenser as well as energy recovery from the first stage. In this case, $\frac{m_{w,2}}{m_w} > 0$, $1 + \frac{m_{w,2}}{m_w} > 1$, and the resulting dual-stage efficiency is greater than that of the first stage alone.

In our analysis, we considered the condenser temperature of S1 to be the same as the desorption temperature of S2. Meanwhile, the condenser temperature of S2 is maintained at 25 °C. Therefore, the four operating temperature nodes in Eq. (15) can be reduced to just two. Fig. 16(a) shows the thermal efficiency map of a MOF-303 based dual-stage AWH device as a function of the desorption temperatures of S1 ($T_{des,1}$) and S2 ($T_{des,2}$) predicted by previous theories.[55] More than 75% of the thermal efficiency map represents a "zero-efficiency zone" [dark-red region in Fig. 16(a)], because the critical desorption temperature is fixed at $\approx 70$ °C when the isotherm-shift is not incorporated. The maximum thermal efficiency of this dual-stage AWH device is only $\approx 0.25$ because only S1 is activated throughout the entire operating temperature range [white boundary in Fig. 16(a)]. Fig. 16(b) shows the thermal efficiency map of a MOF-303 based dual-stage AWH device as a function of the desorption temperatures of S1 and S2 considering the isotherm-shift. In comparison with Fig. 16(a), the "zero-efficiency zone" reduced to only 30% of the entire thermal efficiency map, indicating a much higher device performance is expected with more realistic adsorption characteristics. This enhanced AWH performance originated from both the increased thermal efficiency of S1 white boundary in Fig. 16(b) and the activation of S2 [white-dashed boundary in Fig. 16(b)]. The maximum thermal efficiency increased to $\approx 0.5$ within the same operating temperature range, twice of the prediction in Fig. 16(a).

Figures 16(c)-(d) highlight the significance of tailoring the adsorption characteristics of the material to further enhance AWH performance. Specifically, Fig. 16(c) shows the thermal efficiency map of a dual-stage AWH device as a function of the desorption temperatures of S1 and S2 when $h_{ad} = 4000$ kJ/kg. By increasing $h_{ad}$, the dual-stage device can operate under most temperature conditions, where the "zero-efficiency zone" is only 5% of the entire thermal

efficiency map. Moreover, higher thermal efficiency up to 0.6 can be achieved, because $h_{\text{ad}} = 4000$ kJ/kg is close to the optimal adsorption enthalpy in the operating temperature range from 60 °C to 100 °C [Fig. 14(a)] and lowers the critical desorption temperature of S2 [white-dashed line in Fig. 16(c)].

With a synergistic optimization of the adsorption characteristics and operating temperatures, we predict the fundamental limit of dual-stage AWH devices [Fig. 16(d)]. As shown in Fig. 14, there is an optimal adsorption enthalpy $h_{\text{ad,optimal}}$ to achieve the peak thermal efficiency for each specific $T_{\text{des}}$, i.e., $h_{\text{ad,optimal}} = f(T_{\text{des}})$ of a single-stage AWH device. We extended this result to a dual-stage device by finding the optimal adsorption enthalpy value for each stage, at given desorption temperatures. First, we divide the temperature domain defined on the thermal efficiency maps shown in Fig. 16 into a finite grid. Each point on the grid represents a pair of desorption temperatures $(T_{\text{des,1}}, T_{\text{des,2}})$ for the two stages of a dual-stage device. To find the combination of adsorption enthalpies ( $h_{\text{ad,optimal1}}$ , $h_{\text{ad,optimal2}}$ ) that leads to maximum dual-stage thermal efficiency at any pair of $(T_{\text{des,1}}, T_{\text{des,2}})$, we plotted thermal efficiency curves as a function of adsorption enthalpy (as shown on Fig. 14(a)) at $T_{\text{des,1}}$ and $T_{\text{des,2}}$, respectively, and obtained the adsorption enthalpy values at the peaks of the two curves $(h_{\text{ad,optimal1}}, h_{\text{ad,optimal2}})$. We then used this $(h_{\text{ad,optimal1}}, h_{\text{ad,optimal2}})$ in Eqs. 12-16 to calculate the optimal dual-stage thermal efficiency at $(T_{\text{des,1}}, T_{\text{des,2}})$. We iterated this process for each pair of $(T_{\text{des,1}}, T_{\text{des,2}})$ over the temperature domain to generate the full two-dimensional thermal efficiency maps shown in Fig. 16. For this case, the "zero-efficiency zone" further reduced to 2% and the maximum thermal efficiency increased to 0.7. Fig. 16(d) shows a significantly increased engineering space compared with Figures 16(a)-(b) to enhance the performance of AWH by optimizing both material adsorption properties and device design.
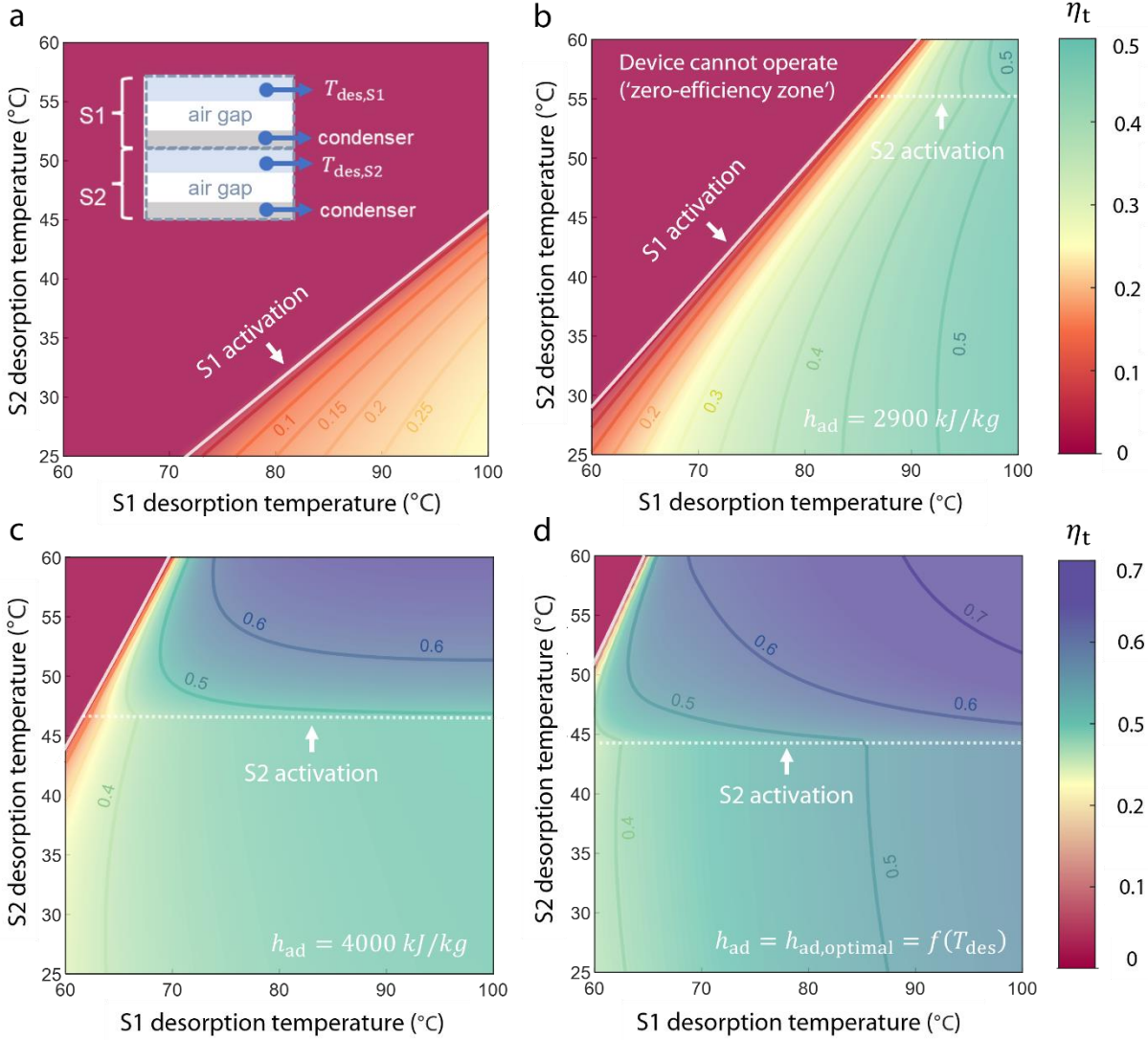
**FIG. 16. Dual-stage thermal efficiency of an AWH device.** Thermal efficiency of dual-stage AWH device as a function of the first (S1) and second (S2) stage desorption temperatures (a) without considering the isotherm-shift, as compared to the improved model that considers the isotherm-shift with temperature when (b) $h_{ad}$ = 2900 kJ/kg, (c) $h_{ad}$ = 4000 kJ/kg, and (d) $h_{ad}$ is set to the optimal value. For each combination of desorption temperatures ($T_{des,1}$, $T_{des,2}$), the optimal value of $h_{ad}$, in the range of 2400 kJ/kg to 4500 kJ/kg, is determined when $\eta_t$ reaches the maximum. The inset of (a) shows a schematic of the dual-stage configuration. In general, three modes are expected for the dual-stage device operation, *i.e.*, no stage activated, only S1 activated, and both S1 and S2 activated. The white-solid line represents the transition from the no stage activated mode to the S1 activated mode, whereas the white-dashed line marks the boundary

between the S1 activated mode and S1 and S2 activated mode. Without considering the isotherm-shift in (a), S2 is not activated throughout the entire temperature range, leading to a large "zero-efficiency zone". In comparison, when the isotherm-shift is considered, S2 can be activated, which leads to a significant enhancement of thermal efficiency up to approximately 0.7.

# Chapter 4: Design of select AWH device subcomponents

## 4.1.   Atmospheric air delivery

The low relative humidity conditions targeted by adsorption-based AWH also makes atmospheric air delivery a non-trivial design problem. Due to the low vapor concentration in arid air, a sufficiently large amount of air needs to be supplied to the adsorbent bed for complete adsorption. This is particularly challenging for next-generation AWH devices with rapid cycling and faster water production, which would require exceptionally high air flow rate. At the same time, the narrow air channels within a compact device create large pressure drops that resist air flow. Furthermore, energy consumption is also a major design constraint for high-performance AWH devices, especially portable ones that operate on limited power supply.

The performance of fans is commonly represented by a fan curve, which relates the outlet pressure drop to the resulting air flow rate generated by the fan. Example fan curves provided by manufacturers are shown in Fig. 17(a). Typically, maximum flow rate is achieved with the 'fully open' case (green dot), where the fan outlet is completely unblocked. On the contrary, maximum static pressure is observed for the 'fully blocked' case (blue dot), where the fan outlet is completely throttled and there is no outgoing flow. Intermediate blockage cases also need to be tested to obtain full curves.  In general, the flow rate decreases with pressure drop for a given fan and power level, and vice versa. This is an essential tradeoff in fan design and selection.

The experimental setup in Fig. 17(b) was built to characterize the aerodynamic performance of fan candidates and obtain fan performance curves. The design principles of this setup were based on the ANSI/AMCA standard 210: Laboratory methods of testing fans for certified aerodynamic performance rating.[69] During the experiments, a candidate fan is placed at the inlet of the air pipe and the accelerated air flows through. The static pressure and flow velocity of the generated air stream are then measured by the downstream static pressure sensor and anemometer, respectively. Measurement instruments for pressure and flow rate were selected based on both accuracy and compatibility with system dimensions. We controlled the extent of throttling and therefore the back static pressure by attaching a disk with variable-diameter holes to the end of the air pipe. This allowed us to swing the testing conditions over the range of the curve.
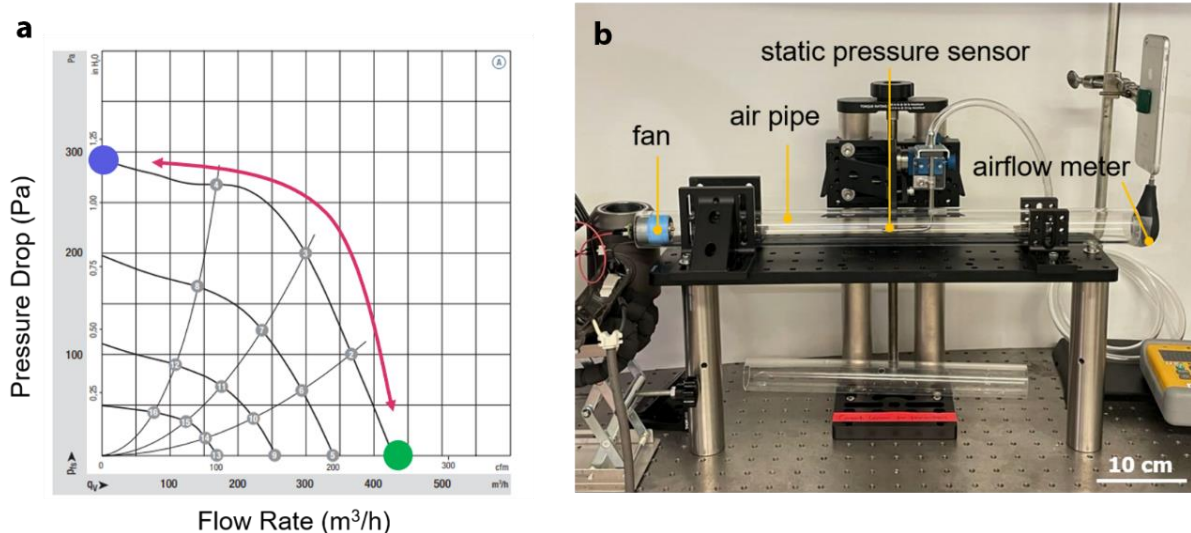
**FIG. 17. Typical fan performance curve and characterization setup.** (a) A typical axial fan performance curve, showing the relation between static pressure and resulting flow rate.[70] (b) Fan performance characterization setup adapted from the ANSI/AMCA standard 210.[69]

Table 4 shows an overview of the various aspects guiding our fan selection. These metrics are evaluated based on our device operation conditions. Maximum mode corresponds to the highest instantaneous air speed over the adsorbent fins needed, 7 m/s, at the beginning of the adsorption cycle. And the average mode corresponds to the nominal speed of 4.5 m/s during later in the cycle. The flow rate and pressure drop are particularly important criteria for the fan selection. We also take the fan configuration, in terms of numbering and spacing, into account for optimized flow distribution, power efficiency, and mass / volume of the fan system.

**TABLE 4. Target fan performance metrics for two device operating modes.**

| Performance metrics | Maximum mode | Average mode |
|---|---|---|
| Speed (m/s) | 7 | 4.5 |
| Flow rate (L/s) | 47.88 | 30 |
| Pressure drop (Pa) | 68 | 43.7 |
| Power efficiency | Target 40% | |

To identify the optimal solution for air delivery, we explored three groups of candidates in parallel [Fig. 18]. (I): Dyson V9 digital integrated motor fan [top left of Fig. 18]. This product is known for combining a powerful motor and optimized fan blades for high performance air delivery, while being extremely compact. However, its complicated control system posed potential challenges for adaptation to portable devices. (II): Commercial brushless DC motors combined with commercial drone propellers [bottom left and center of Fig. 18]. The decoupling of motor and fan gives us more flexibility in tailoring the fan power and form factor to our own application and more closely engages with system integration. Miniature drone motors are also generally small and powerful. (III): Direct current (DC) case fans [right column of Fig. 18] are also good options because of their compact form and easy electrical connections.



**FIG. 18. Summary of motor and fan candidates for high-efficiency air delivery.** Three groups of solutions were explored in parallel. (I): Dyson V9 digital integrated motor fan. (II): Commercial brushless DC motors combined with commercial drone propellers. (III): DC computer case fans.

### 4.1.1. Dyson V9 integrated motor fan.

We first evaluated the feasibility of using the Dyson V9 integrated motor fan for delivering air to the adsorption beds. The Dyson V9 stood out as a strong candidate initially because it was expected to deliver a high flow rate of up to 30 L/s, while being small and lightweight. We were able to successfully extract the V9 motor fan from the original Dyson product. Figures 19(a)-(b) show the heating element and control board from the original product. They were electronically connected to the V9 motor fan, which is shown in Figures 19(c)-(d).

We then attempted to reconnect the extracted motor fan back to an external electrical circuit for power and control. This turned out to be a major technical barrier. Figure 19(e) shows a schematic of the circuit modification we attempted. A major operation involved electrically removing the unneeded heating element and reconnecting the interrupted circuit. We then attempted to power the circuit with an AC (120V 60Hz) power source and use the control board to send out a varying DC signal to the motor fan. However, this method failed after repeated attempts.
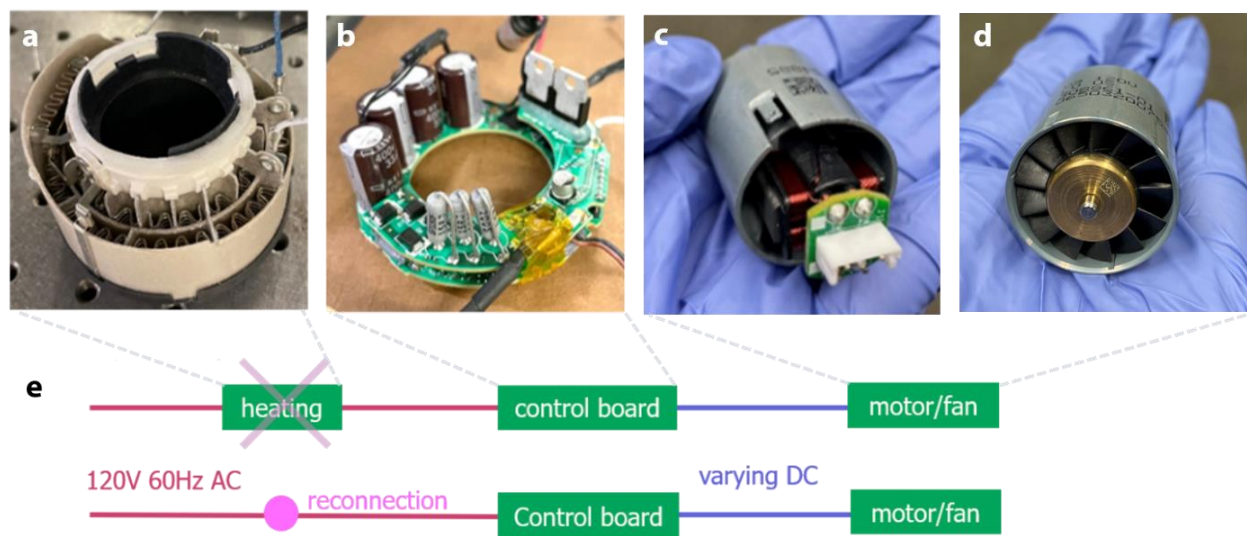


**FIG. 19. Circuit modification of Dyson V9 motor fan.** (a) Original heating elements. (b) Original control board. (c)-(d) Rear and front views of the extracted Dyson V9 compact motor fan. (e) Electrical circuit modification of the Dyson V9 motor fan for operate outside the original product, without the heating elements.

We then investigated the working principle of the motor together with a group of motor experts at MIT and identified a possible mechanism as follows: the motor consists of a high-performance

permanent magnet rotor and a single-phase electromagnet stator. The stator is unevenly shaped to create a magnetic offset that ensures starting rotation in the right direction. A position sensor on the rotor sends feedback to the control board, which then sends electrical signals controlling the electromagnetic phase of the stator. The control board powers the motor and maintains dynamically optimized phase relations for continuous rotation. It is therefore infeasible to operate the motor with any standard wave forms e.g., AC, DC, PWM, without its original controller. A dynamic feedback control signal is essential for controlling the electromagnet stator correctly. However, the as-programmed controller detects input power and only accepts AC source of at least 80V. It also does not allow voltage variation for tuning the fan RPM to specific applications. Reprogramming of the controller board would also be highly challenging due to proprietary restrictions. We hence concluded that the Dyson V9 motor fan does not align with the capabilities and limitations of the power unit of our system, or any small portable device in general.

### 4.1.2. Miniature drone propellers

Motorized drone propellers combine the advantages of compact form, optimizable components, and high air flow rate. Furthermore, they usually belong to the brushless DC type that can be easily powered by DC power supply in lab or battery packs on a portable device. These aspects make drone motors and propellers promising candidates for high-performance AWH devices.

Advanced racing motors generally have a 3-phase (instead of single phase) electromagnet stator for enhanced thrust and more continuous rotation of the permanent magnet rotor. This requires a complimentary ESC control unit to provide the 3-phase electrical relay to the stator. A demo of the electrical circuit constructed for powering and controlling the speed of 3-phase electric drone motors is shown in Fig. 20.
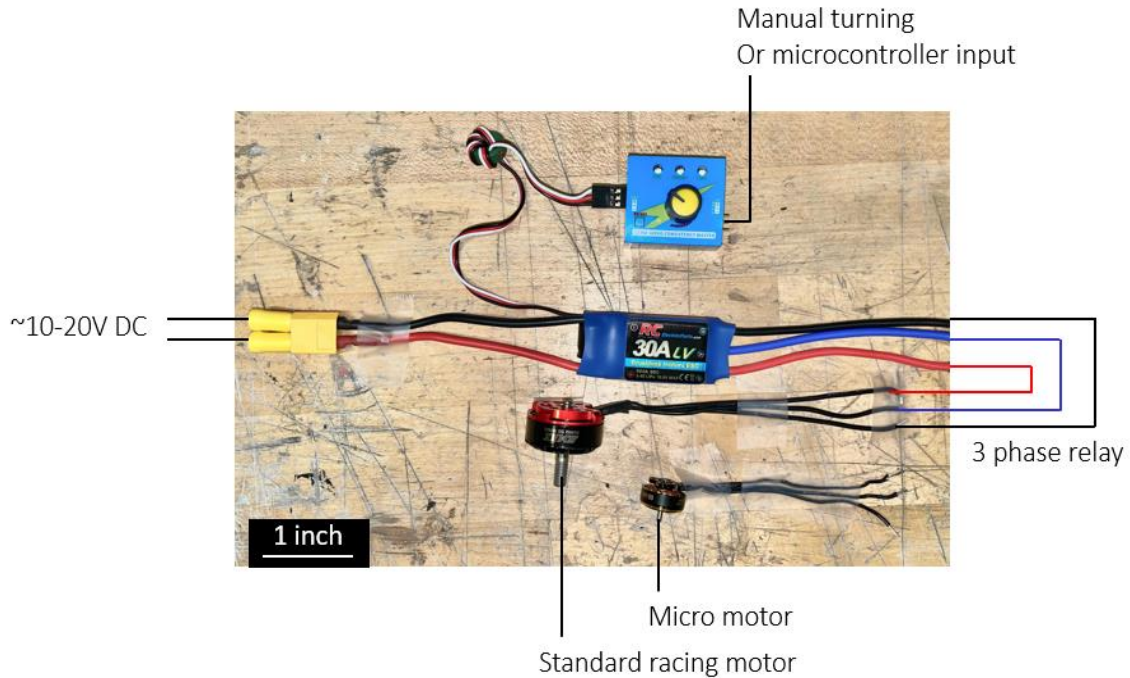
**FIG. 20. Electrical circuit for testing 3-phase drone motors.**

There are two main grades of compact drone motors: the regular FPV racing type, and the smaller, micro type. We plan to investigate two candidates under each group, for a total of four initial candidates. We identify them as motors S1, S2, M2, M1, in the order of decreasing size (S for 'standard; M for 'Micro'). Table 5 summarizes more detailed specifications of each candidate. In terms of propeller pairing, the regular-type motors work best with propellers of 3-5" in diameter, whereas the micro-type works well with 2-3" diameter props. The combined effects of power intake, motor RPM, propeller shape and size will dictate the final air propulsion performance and our component selection.

**TABLE 5. Specifications of drone micromotor candidates.**

| | FPV Racing (Regular) | | Micro motor (Smaller) | |
|---|---|---|---|---|
| Candidate model | EMAX RS2205 | T-Motor F1507 | EMAX RS1106 | T-Motor F1103 |
| Identifier | S1 | S2 | M2 | M1 |
| | | | | |
| KV rating | 2300 KV | 3800 KV | 6000 KV | 8000 KV |
| Max. thrust | +1000 g | 673 g | unreported | 235.47 g |
| Outer diameter | ~ 30 mm | | ~ 20 mm | |
| Bearing size | 5 mm | | 1.5 mm | |
| Propeller size | 3-5" | | 2-4" | |

\* KV = unloaded RPM per volt of power input.

A mechanical setup was also developed for characterizing air delivery performances of drone motors and propellers. Figure 21 illustrates the mounting of a micro motor and propeller combination on the apparatus and highlights some key instruments. The new laser-cut motor mounts are more streamlined to reduce interference with the air flow. The pipe dimension is also adjusted to match much more closely with the propeller dimensions. The reduced gap between the propeller tip and the pipe wall is expected to lower aerodynamic loss and improve power efficiency. Fig. 21(c)-(d) show the upgrade from a vane-type anemometer previously used for case fan testing, to a probe-type hotwire anemometer. The latter interferes less with the flow field and is expected to yield more accurate flow speed measurements. For initial testing, center-hole throttle plates [Fig. 21(e)] were used to vary the back pressure and change the operating point.
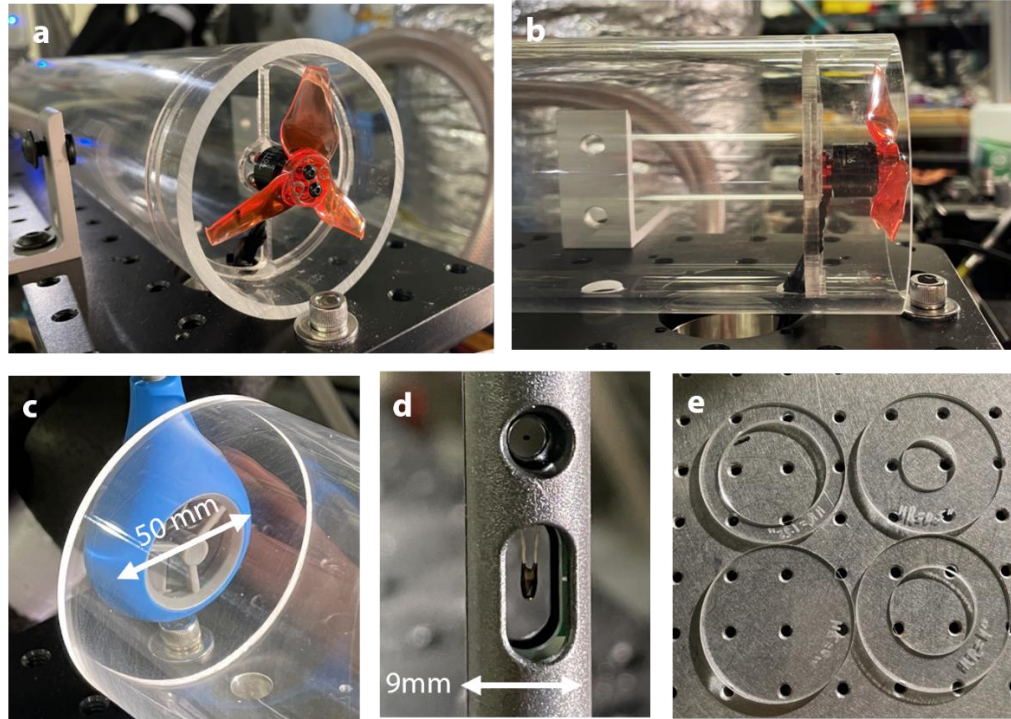
**FIG. 21. Key components of the characterization setup for motorized drone propellers.** (a)-(b) Front and side views of a small drone propeller mounted at the air inlet. (c) A vane-type anemometer blocking a large area of the outlet. (d) Close-up image of the sensing elements of a hotwire anemometer. (e) Center-hole throttle plates.

To improve mechanical resolution and electrical stability, we further upgraded the characterization setup. First, we achieved much more stable electrical connection between electronic motor and its control elements using a compression wire nut [Fig. 22(a)]. Traditional wire connection techniques such as soldering, and heat shrink tubing introduced occasional connection loss previously. This is primarily due to the significant wire dimension mismatch between the motor (small) and the controller (large). The motor wires also appeared non-wetting to the soldering materials. Secondly, we fabricated new throttle plates with slit openings, as shown in Fig. 22(b). This helped ensure more uniform flow within the measurement tube, which enabled better sensing of the flow rate and pressure with point probes. Multiple plates can be used in combination to create additional throttle patterns [Fig. 22(c)]. Using the latest setup, initial performance curves for a micromotor and 2.3" propeller combination was measured for the base case of low current draw up to 2A [Fig. 22(d)]. The preliminary results demonstrated our success with operating and varying the speed of

the drone propulsion unit, as well as its capability to generate high flow rate at relatively high back pressure resistance as compared to standard case fans of similar dimensions.
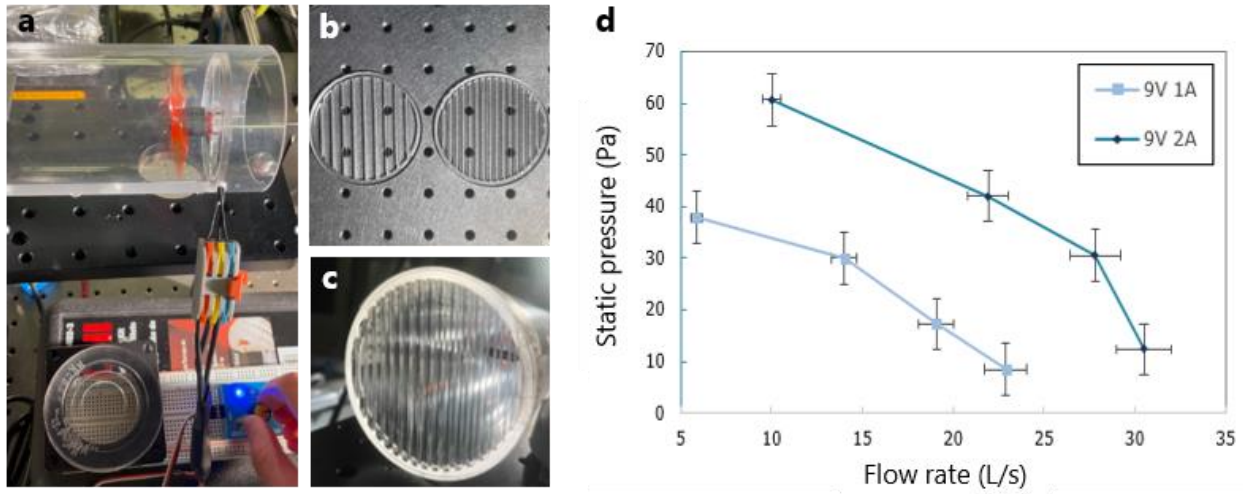


**FIG. 22. Upgraded setup and preliminary results of drone propeller characterization.** (a) Improved electrical connection between the motor and controller using a compression wire nut. (b)-(c) New throttle plates with slit openings to ensure more uniform air flow. (d) Preliminary performance curves of a 2.3" propeller an M1 motor, characterized using the upgraded setup.

### 4.1.3. Noctua industrial DC case fan

Some industrial DC fans are known for their high-speed air flow and excellent energy efficiency. Specifically, we focused on testing industrial Fan (NF A14-3000) which showed promising results especially in terms of power consumption. The maximum power consumption per fan was 6.6 W.

As shown in Fig. 23(a), we tested the fan using our in lab-built fan setup to generate the fan curves at five different conditions: (I) fully open, 3 cases of partially closed [(II) coarse – (III) fine – (IV) very fine mesh], and (V) fully closed, which correspond to the five data points per fan curve. As shown in Fig. 23(a), our setup consisted of two sensors: a hotwire anemometer and a static pressure pitot tube. Hotwire anemometer measured the velocity of air inside the (148 x 148 mm) duct, which helped in quantifying the total volumetric air flow rate (Q), while the pitot tube measured the static pressure. The operational efficiency (η) was evaluated by taking the ratio of the actual power, which is the product of the volumetric flow rate and total pressure drop (static and dynamic pressure drop) to the total power input. The total power input is the product of the voltage and

current consumed by the fan during operation. The following expression was used to estimate the fan efficiency,

$$\eta = \frac{Q \Delta P_{tot}}{VI}. \tag{17}$$

As shown in Fig. 23(b), the fan curve varied significantly with the PWM. The input power is the product of the PWM and the maximum power consumption, 6.6 W. Since the fan was designed for high-speed operations, the efficiency increased with the flow rate. Additionally, this fan also provides a much more silent operation compared to the drone motors. Operating the fan at 5 W, i.e., PWM = 75%, can achieve a high fan efficiency of about 35% [star symbol in Fig. 23(b)]. This is very close to the target efficiency of 40% and significantly higher than the efficiencies of other candidates discussed previously.
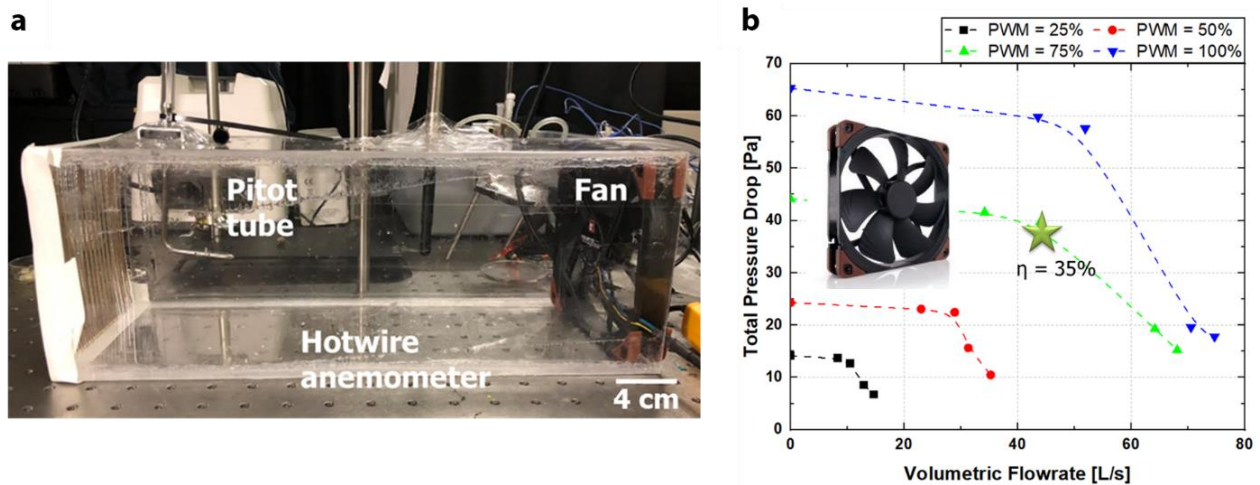


**FIG. 23. Noctua industrial DC case fan characterization.** (a) The fan characterization setup built in the lab for Noctua NF A14-3000 industrial DC case fan. A 148 mm x 148 mm duct was constructed where the fan was fixed at the entrance. Air velocity was measured by a hotwire anemometer and the static pressure was measure by the pitot tube. (b) Fan curves of NF A14-3000 at various PWM levels ranging from 100% to 25%.

In summary, all three groups of candidate fans demonstrated exceptional performance in terms of air flow rate and pressure drop, as compared to common USB fans. The Dyson V9 motor fan and drone propeller fan tested were particularly compact and powerful relative to their sizes. However, both solutions were compromised by their complex control system and low power efficiency. The

Noctua industrial case fan (NF A14-3000) emerged as the best overall candidate that met all target air delivery metrics for high-performance AWH devices. It combined the benefits of high flow performance, lightweight and ease to use.

## 4.2  Condenser

The condenser is also a critical component of an AWH device, as it dictates the rate of water vapor condensation and latent heat rejection. To guide condenser design, we performed baseline modeling of the condenser heat transfer performance and water retention during desorption. Any water retained on condenser will not be collected in the water container.

Condensation could be either filmwise or dropwise, depending on the surface properties of the condenser. During filmwise condensation, water forms a thin film that could inhibit the overall heat transfer coefficient (HTC) as thickness of the film increases. Figure 24 shows the effect of vapor condensation rate on the condensed water film thickness, HTC, and temperature rise on the condenser. The expected condensation rates corresponding to the operating range of a currently under-development device [shaded boxes in Figures 24(a)-(b)] were calculated and used to determine the water film thickness, expected HTC and temperature rise. The current estimations showed acceptable water film thickness and average HTC at the minimum condensation rate [green circles on Fig. 24(a)]. However, the temperature rise on the condenser (as compared to ambient temperature) was predicted to be over 20°C even for the lower-bound condensation rate. This result suggested large enhancement potential for the heat sink design on the back side of the condenser,
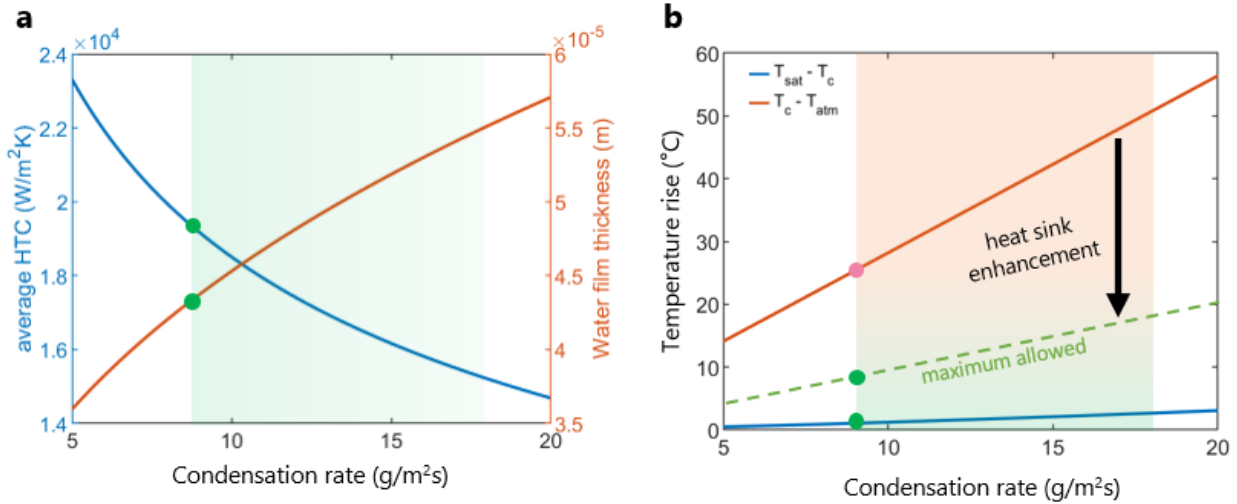
**FIG. 24. Nusselt prediction of the heat transfer performance of a condenser with filmwise condensation.** (a) The condensed water film thickness and average HTC as a function of condensation rate. (b) The temperature rise on the condenser as a function of condensation rate.

Dropwise condensation, on the other hand, could provide higher thermal performance but may have a larger water retention. This is possible at the early stage of the condensation even when the surface is hydrophilic. Therefore, we investigated the force balance of a water droplet on a sloped surface to better understand the phenomenon.[71,72] The two main forces acting on a droplet are down-pulling gravity and up-lifting surface tension. When the droplet begins to slide, the gravity term exceeds the surface tension. In our design, the condenser will be placed vertically, which is beneficial for minimizing the water retention. The water retention occurs mainly due to the contact angle hysteresis. For industrial hydrophilic surfaces, the delta theta ranges from 20 to 60 degrees, causing the water retention. Previous literature reported droplet spraying experiments with a wide range of surfaces and liquid.[72] The analysis and experimental results provide us a valuable guidance in our condenser design.

Based on a range of surface contact angles and hysteresis, we estimated the respective water retention amount, as shown in Fig. 25. Compared to the 30mL water we expect to collect per condenser and per cycle, there is a design space to minimize the water retention. Unfortunately, some of the contact angle hysteresis is not widely available for most commercial products. In the future, we will search for available condenser options, with water retention as one important criterion.
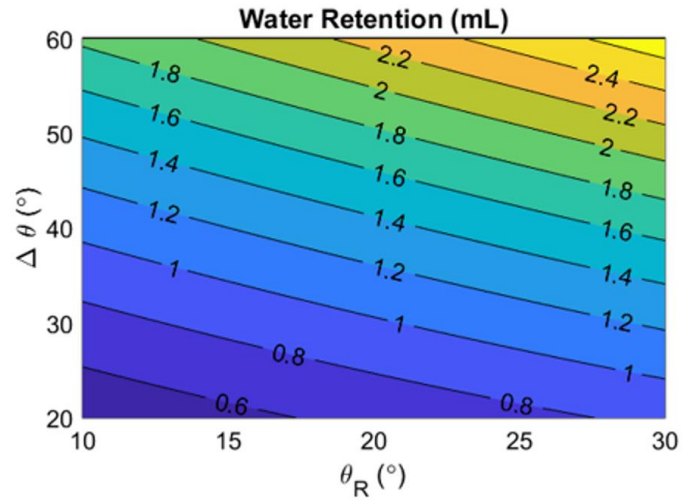
**FIG. 25. Water retention estimation on the condenser surface.** The amount of water retention is plotted as a function of the nominal contact angle and the contact angle hysteresis of droplets on the condenser surface.

# Chapter 5: Conclusions and future work

## 5.1. Conclusions

In this thesis, we developed a generalized thermodynamic model for adsorption based AWH devices that considers the temperature-dependence of adsorption. We identified that the expected adsorption isotherm-shift with temperature is a critical phenomenon to describe the interaction between adsorbent characteristics and operating conditions. We showed that the fundamental limits of AWH can exceed those predicted by previous models due to the isotherm-shift. More importantly, we demonstrated that there is an optimal desorption temperature and adsorption enthalpy to achieve the highest thermal efficiency of an AWH device, which is a result of the interplay between desorption and sensible heating in the adsorption beds. Our analysis not only enables the determination of optimal operating conditions for AWH devices, but also guides the adsorbent selection and tailoring adsorbent materials for realistic operating constraints.

For atmospheric air delivery, all three groups of candidate fans demonstrated exceptional performance in terms of flow rate and overcoming pressure drops, as compared to common USB fans. The Dyson V9 motor fan and motorized drone propellers tested were particularly compact and powerful relative to their sizes. However, both solutions were compromised by their complex control system and low power efficiency. The Noctua industrial case fan (NF A14-3000) ultimately emerged as the best overall candidate as it combined the benefits of high flow performance, lightweight and ease to use. These cover all primary air delivery metrics for high-performance AWH devices. Lastly, our preliminary condenser model showed reasonable heat transfer performances based on the Nusselt prediction for filmwise condensation, suggesting potential enhancement of the heat sink for improved cooling. We also estimated the amount of water retention on the condenser as a function of the surface contact angle and hysteresis, and observed that the amount is generally small.

## 5.2. Future work

Future opportunities for the improved AWH thermodynamic model proposed here include enabling more accurate predictions on the global potential for harvesting water from the air, as well as providing the theoretical basis for a potential three-stage AWH device.

The scope and applicability of the model could be further enhanced with several potential generalizations. For instance, current models have focused on adsorbents with highly idealized step-shaped isotherms. Extensions to other types of isotherms could be valuable for modeling a broader range of adsorbents with more realistic characteristics. In addition, many materials exhibit general sorption behaviors that involve both adsorption and absorption. Hydroscopic hydrogel is an example of such materials and has shown potential for scalable water harvesting from the air. Yet, device-level thermodynamic modeling on advanced sorption-based systems (e.g. hydrogel thermal storage) remains lacking.

To approach the fundamental limits predicted by thermodynamic analysis, it is also critical to develop high-fidelity multi-physics models that capture the kinetics and transport losses associated with real devices. Lastly, major breakthroughs in the scale-up of advanced adsorbents and device subcomponents are needed to realize the global potential of AWH technologies.

# Bibliography

1.   Gosling, S. N. & Arnell, N. W. A global assessment of the impact of climate change on water scarcity. doi:10.1007/s10584-013-0853-x.

2.   Boretti, A. & Rosa, L. PERSPECTIVE Reassessing the projections of the World Water Development Report. doi:10.1038/s41545-019-0039-9.

3.   LaPotin, A. D. Multi-stage adsorption-based atmospheric water harvesting. (2019).

4.   Mekonnen, M. M. & Hoekstra, A. Y. Sustainability: Four billion people facing severe water scarcity. *Sci. Adv.* **2**, (2016).

5.   Water and Sanitation - United Nations Sustainable Development. https://www.un.org/sustainabledevelopment/water-and-sanitation/.

6.   UN Water. Report 4: Managing Water under Uncertainty and Risk (Vol. 1), Knoledge Base (Vol. 2) and Facing the Challenges (Vol. 3). **1**, 867 (2012).

7.   A Comprehensive Assessment of Water Management in Agriculture. (2007).

8.   Rijsberman, F. R. Water scarcity: Fact or fiction? *Agric. Water Manag.* **80**, 5–22 (2006).

9.   Postel, S. L., Daily, G. C. & Ehrlich, P. R. Human Appropriation of Renewable Fresh Water. *Science (80-. ).* **271**, 785–788 (1996).

10.  Savenije, H. H. G. Water scarcity indicators; the deception of the numbers. *Phys. Chem. Earth, Part B Hydrol. Ocean. Atmos.* **25**, 199–204 (2000).

11.  Liu, J. *et al.* Water scarcity assessments in the past, present and future. *Earth's Futur.* **5**, 545 (2017).

12.  Vörösmarty, C. J., Green, P., Salisbury, J. & Lammers, R. B. Global Water Resources: Vulnerability from Climate Change and Population Growth. *Science (80-. ).* **289**, 284–288 (2000).

13.  Ercin, A. E. & Hoekstra, A. Y. Water footprint scenarios for 2050: A global analysis. *Environ. Int.* **64**, 71–82 (2014).

14.  Arnell, N. W., van Vuuren, D. P. & Isaac, M. The implications of climate policy for the impacts of climate change on global water resources. *Glob. Environ. Chang.* **21**, 592–603 (2011).

15.  Mancosu, N., Snyder, R. L., Kyriakakis, G. & Spano, D. Water Scarcity and Future Challenges for Food Production. **7**, 975–992 (2015).

16.  Water Scarcity | Threats | WWF. https://www.worldwildlife.org/threats/water-scarcity.

17.  Water scarcity | UNICEF. https://www.unicef.org/wash/water-scarcity.

18.  Effects Of The Water Crisis On Health | Water.org. https://water.org/our-impact/water-crisis/health-crisis/.

19. Dolan, F. *et al.* Evaluating the economic impact of water scarcity in a changing world. doi:10.1038/s41467-021-22194-0.

20. Humphrey, J. H. *et al.* The potential for atmospheric water harvesting to accelerate household access to safe water. (2020) doi:10.1016/S2542-5196(20)30034-6.

21. Liu, X., Beysens, D. & Bourouina, T. Water Harvesting from Air: Current Passive Approaches and Outlook. *ACS Mater. Lett.* 1003–1024 (2022) doi:10.1021/ACSMATERIALSLETT.1C00850/ASSET/IMAGES/LARGE/TZ1C00850_0012.JPEG.

22. Li, Z. *et al.* Solar-Powered Sustainable Water Production: State-of-the-Art Technologies for Sunlight-Energy-Water Nexus. *ACS Nano* **15**, 12535–12566 (2021).

23. Zhou, X., Lu, H., Zhao, F. & Yu, G. Atmospheric Water Harvesting: A Review of Material and Structural Designs. *ACS Mater. Lett.* **2**, 671–684 (2020).

24. Kim, H. *et al.* Adsorption-based atmospheric water harvesting device for arid climates. doi:10.1038/s41467-018-03162-7.

25. Tu, Y., Wang, R., Zhang, Y. & Wang, J. Progress and Expectation of Atmospheric Water Harvesting. *Joule* **2**, 1452–1475 (2018).

26. Li, R., Shi, Y., Wu, M., Hong, S. & Wang, P. Improving atmospheric water production yield: Enabling multiple water harvesting cycles with nano sorbent. *Nano Energy* **67**, (2020).

27. Lu, H. *et al.* Materials Engineering for Atmospheric Water Harvesting: Progress and Perspectives. *Adv. Mater.* **34**, (2022).

28. Ejeian, M. & Wang, R. Z. Adsorption-based atmospheric water harvesting. *Joule* **5**, 1678–1703 (2021).

29. Adsorption - Jozsef Toth - Google Books. https://books.google.com/books?hl=en&lr=&id=lTMzpP1lcpkC&oi=fnd&pg=PR3&dq=adsorption&ots=4V1rhGa97H&sig=gAYoDeMOEmsWAk4oFN6aLTflIEY#v=onepage&q=adsorption&f=false.

30. Dąbrowski, A. Adsorption — from theory to practice. *Adv. Colloid Interface Sci.* **93**, 135–224 (2001).

31. Adsorption Technology and Design - W John Thomas, FEng, Barry Crittenden - Google Books. https://books.google.com/books?hl=en&lr=&id=tXOqBBn8m-sC&oi=fnd&pg=PA7&dq=adsorption&ots=gafR7RdWJ1&sig=eudX1_RkqpRFtyN4wTI9jcsrDpo#v=onepage&q=adsorption&f=false.

32. Principles of Adsorption and Adsorption Processes - Douglas M. Ruthven - Google Books. https://books.google.com/books?hl=en&lr=&id=u7wq21njR3UC&oi=fnd&pg=PR17&dq=adsorption&ots=wcYnPnAdrX&sig=AQdVXvYAgZ5EzVHEL_cUSoJzUgc#v=onepage&q=adsorption&f=false.

33. Glossary | Publications and Other Information | BTSC. https://web.archive.org/web/20080218094403/http://www.brownfieldstsc.org/glossary.cfm?q=1.

34. LaPotin, A. *et al.* Dual-Stage Atmospheric Water Harvesting Device for Scalable Solar-Driven Water Production. *Joule* **5**, 166–182 (2021).

35. Nemiwal, M. & Kumar, D. Metal organic frameworks as water harvester from air: Hydrolytic stability and adsorption isotherms. *Inorg. Chem. Commun.* **122**, (2020).

36. Rieth, A. J. *et al.* Record-Setting Sorbents for Reversible Water Uptake by Systematic Anion Exchanges in Metal-Organic Frameworks. *J. Am. Chem. Soc.* **141**, 13858–13866 (2019).

37. Hyunho, K. K. *et al.* Water harvesting from air with metal-organic frameworks powered by natural sunlight. *Science (80-. ).* **434**, 430–434 (2017).

38. Hanikel, N. *et al.* Rapid Cycling and Exceptional Yield in a Metal-Organic Framework Water Harvester. *ACS Cent. Sci.* **5**, 1699–1706 (2019).

39. Logan, M. W., Langevin, S. & Xia, Z. Reversible Atmospheric Water Harvesting Using Metal-Organic Frameworks. *Sci. Rep.* **10**, 1492 (2020).

40. Rieth, A. J., Yang, S., Wang, E. N. & Dincă, M. Record Atmospheric Fresh Water Capture and Heat Transfer with a Material Operating at the Water Uptake Reversibility Limit. *ACS Cent. Sci.* **3**, 668–672 (2017).

41. Kim, H. *et al.* Water harvesting from air with metal-organic frameworks powered by natural sunlight. *Science (80-. ).* **356**, 430–434 (2017).

42. Burtch, N. C., Jasuja, H. & Walton, K. S. Water stability and adsorption in metal-organic frameworks. *Chem. Rev.* **114**, 10575–10612 (2014).

43. Terzis, A. *et al.* High-Frequency Water Vapor Sorption Cycling Using Fluidization of Metal-Organic Frameworks. *Cell Reports Phys. Sci.* **1**, (2020).

44. Tingting, P., Kaijie, Y. & Yu, H. Recent Progress of Atmospheric Water Harvesting Using Metal-Organic Frameworks. *Chem. Res. Chinese Univ.* **2020**, 33–40.

45. Darunte, L. A., Oetomo, A. D., Walton, K. S., Sholl, D. S. & Jones, C. W. Direct Air Capture of CO2 Using Amine Functionalized MIL-101(Cr). *ACS Sustain. Chem. Eng.* **4**, 5761–5768 (2016).

46. Li, X. *et al.* Zeolite y adsorbents with high vapor uptake capacity and robust cycling stability for potential applications in advanced adsorption heat pumps. *Microporous Mesoporous Mater.* **201**, 151–159 (2015).

47. Lapotin, A., Kim, H., Rao, S. R. & Wang, E. N. Adsorption-Based Atmospheric Water Harvesting: Impact of Material and Component Properties on System-Level Performance. (2019) doi:10.1021/acs.accounts.9b00062.

48. Cmarik, G. E., Kim, M., Cohen, S. M. & Walton, K. S. Tuning the Adsorption Properties of UiO-66 via Ligand Functionalization. (2012) doi:10.1021/la3035352.

49.   Jasuja, H., Zang, J., Sholl, D. S. & Walton, K. S. Rational Tuning of Water Vapor and CO 2 Adsorption in Highly Stable Zr-Based MOFs. (2012) doi:10.1021/jp308657x.

50.   Gordeeva, L. G. *et al.* Metal-organic frameworks for energy conversion and water harvesting: A bridge between thermal engineering and material science. *Nano Energy* **84**, 105946 (2021).

51.   Hua, L., Xu, J. & Wang, R. Exergy-efficient boundary and design guidelines for atmospheric water harvesters with nano-porous sorbents. *Nano Energy* **85**, (2021).

52.   Burhan, M., Shahzad, M. W. & Ng, K. C. A Universal Theoretical Framework in Material Characterization for Tailored Porous Surface Design. *Sci. Rep.* **9**, 1–7 (2019).

53.   Fundamental thermodynamic properties of sorbents for atmospheric water capture. *Chem. Eng. J.* **431**, 134058 (2022).

54.   Tu, R., Liu, M., Wang, S. & Yang, X. Performance analyses and optimizations of desiccant wheel-assisted atmospheric water harvesting systems based on ideal thermodynamic cycles. *Energy Convers. Manag.* **245**, (2021).

55.   Kim, H., Rao, S. R., LaPotin, A., Lee, S. & Wang, E. N. Thermodynamic analysis and optimization of adsorption-based atmospheric water harvesting. *Int. J. Heat Mass Transf.* **161**, 120253 (2020).

56.   Lord, J. *et al.* Global potential for harvesting drinking water from air using solar energy. *Nature* **598**, 611–617 (2021).

57.   Demir, H., Mobedi, M. & Ülkü, S. A review on adsorption heat pump: Problems and solutions. *Renew. Sustain. Energy Rev.* **12**, 2381–2403 (2008).

58.   Xu, Z. & Wang, R. High-Performance Absorption Thermal Storage with Once-Through Discharging. *ACS Sustain. Chem. Eng.* **10**, 720–730 (2022).

59.   Wahlgren, R. V. Atmospheric water vapour processor designs for potable water production: a review. *Water Res.* **35**, 1–22 (2001).

60.   Narayanan, S., Yang, S., Kim, H. & Wang, E. N. Optimization of adsorption processes for climate control and thermal energy storage. *Int. J. Heat Mass Transf.* **77**, 288–300 (2014).

61.   Jiang, Y., Bagheri, M. H., Loibl, R. T. & Schiffres, S. N. Thermodynamic limits of adsorption heat pumps: A facile method of comparing adsorption pairs. *Appl. Therm. Eng.* **160**, 113906 (2019).

62.   Rahman, S. *et al.* Temperature dependence of adsorption hysteresis in flexible metal organic frameworks. *Commun. Chem.* **3**, 3–8 (2020).

63.   Li, G. K. *et al.* Temperature-regulated guest admission and release in microporous materials. *Nat. Commun.* **8**, 1–9 (2017).

64.   Kim, H. *et al.* Characterization of Adsorption Enthalpy of Novel Water-Stable Zeolites and Metal-Organic Frameworks. *Sci. Rep.* **6**, 1–8 (2016).

65.   Fathieh, F. *et al.* Practical water production from desert air. *Sci. Adv.* **4**, 1–10 (2018).

66.     Gertsbakh, I. *Measurement Theory for Engineers*. *Measurement Theory for Engineers* (Cambridge University Press, 2003).

67.     Nuhnen, A. & Janiak, C. A practical guide to calculate the isosteric heat/enthalpy of adsorption: Via adsorption isotherms in metal-organic frameworks, MOFs. *Dalt. Trans.* **49**, 10295–10307 (2020).

68.     Siperstein, F. R., Avendaño, C., Ortiz, J. J. & Gil-Villegas, A. Analytic expressions for the isosteric heat of adsorption from adsorption isotherm models and two-dimensional SAFT-VR equation of state. *AIChE J.* **67**, e17186 (2021).

69.     Laboratory Methods of Testing Fans for Certified Aerodynamic Performance Rating STANDARD. (2016).

70.     Fans and gear motors for solid fuel heating systems Quiet and reliable output in compact design.

71.     Wang, C. *et al.* Dynamic contact of droplet with superhydrophobic surface in conditions favour icing. *J. Phys. Conf. Ser.* **530**, 012028 (2014).

72.     Furmidge, C. G. L. Studies at phase interfaces. I. The sliding of liquid drops on solid surfaces and a theory for spray retention. *J. Colloid Sci.* **17**, 309–324 (1962).

73.     Díaz-Marín, C. D. *et al.* Kinetics of Sorption in Hygroscopic Hydrogels. *Nano Lett.* **22**, 1100–1107 (2022).